APPROVAL SHEET

Title of Document: A STUDY OF POLARIZATION ATTRACTION: THE FIRST APPLICATION TO A BPSK SIGNAL AND AN EVALUATION OF ROBUSTNESS TO TRANSMISSION IMPAIRMENTS.

Name of Candidate: Aaron DeLong
Doctor of Philosophy, 2018

Signature:
Dissertation and Abstract Approved: Dr. Gary M. Carter
Professor of Computer Science and Electrical Engineering Department

Date Approved: _____

ABSTRACT

Title of Document: A STUDY OF POLARIZATION ATTRACTION: THE FIRST APPLICATION TO A BPSK SIGNAL AND AN EVALUATION OF ROBUSTNESS TO TRANSMISSION IMPAIRMENTS.

Aaron DeLong, Doctor of Philosophy, 2018

Directed By: Dr. Gary M. Carter
Professor of Computer Science and Electrical Engineering Department

This thesis is a study of polarization attraction (PA), an all-optical polarization regeneration technique. PA is one implementation of a nonlinear lossless polarizer (NLP) that has demonstrated success for pulse train and OOK signals with a high optical signal-to-noise ratio (OSNR). Before PA may be realized as a useful or realistic application for a long-haul transmission system, first it must be experimentally demonstrated as a potential application for phase-shift keyed (PSK) signals. In addition, its robustness to transmission impairments, such as accumulated amplified spontaneous emission (ASE) or nonlinearities, would also need to be evaluated. Hence, this work aims to accomplish both benchmarks for PA to test its efficacy in a more realistic long-haul transmission system. First, an investigation was carried out for the counter-propagating beam configuration of PA employed for a 10.7-GBaud non-return-to-zero binary-phase-shift-keyed (NRZ-BPSK) signal in a highly nonlinear fiber (HNLF) by using the Kerr nonlinear cross-polarization process inherent to that fiber. The receiver sensitivity penalty at the G.709.1 forward error correction (FEC) threshold (bit-error-rate ~ $3.8 \cdot 10^{-3}$) relative to the baseline NRZ-

BPSK signal was negligible, when PA was employed and a degree of polarization (DOP) > 90% was achieved. These results are the first to confirm that PA may be employed for BPSK signals. Next, a coherent reception investigation was carried on PA of a 10.7-GBaud NRZ-BPSK signal pre-loaded with ASE. For this ASE-loaded PA experiment the receiver sensitivity penalty at the G.709.1 FEC threshold, was found to be ≈ 10.5 dB relative to the baseline performance. The final and most complex experiment investigates PA after long-haul 100-GHz DWDM transmission in a recirculating loop. PA on a signal after ~2,400km of transmission was found to achieve approximately the same DOP and receiver sensitivity performance, as that of ASE-loaded PA experiment. The last two experiments lead to the conclusion that the interactions of ASE and fiber nonlinearity, due to the Gordon-Mollenauer effect within the attraction medium, dominate other impairments including those arising in the DWDM transmission.

A STUDY OF POLARIZATION ATTRACTION: THE FIRST APPLICATION TO A BPSK SIGNAL AND AN EVALUATION OF ROBUSTNESS TO TRANSMISSION IMPAIRMENTS.

By

Aaron DeLong

Dissertation submitted to the Faculty of the Graduate School of the
University of Maryland, Baltimore County in partial fulfillment
of the requirements for the degree of
Doctor of Philosophy
2018

Advisory Committee:

Professor Gary M. Carter
Professor Tinoosh Mohsenin
Professor Terrance Worchesky
Dr. William Astar
Dr. Brice Cannon

Acknowledgements

First, I would like to give my deepest thanks to my advisor, Dr. Gary Carter, for his invaluable guidance and support while pursuing my doctoral degree. Through unexpected twists and struggles, his generous patience and encouragement kept me focused on my goal. For these reasons, I would like to express my sincere gratitude to him for this achievement.

I would also like to thank Dr. Astar for his generous mentorship in all skills ranging from technical experimental procedures to workplace professionalism. In addition, this dissertation includes a theoretical section, developed to partially corroborate the experimental results, and is ascribed to Dr. Astar.

I would like to thank Dr. Brice Cannon and Dr. Tanvir Mahmood, for their valuable contributions to this work. I would also like to thank them both for their leadership and camaraderie during my early days at LPS, and for their helpful continued support, advice, and guidance beyond LPS.

I would like to thank the group at LPS and the University of Maryland, for providing this opportunity to work in their facilities on a variety of interesting projects.

I would like to express my gratitude to Dr. Tinoosh Mohsenin and Dr. Terrance Worchesky, for lending their expertise to this work and serving as honorable members of my dissertation committee.

Finally, I would like to give thanks to my family and my friends for their consistent support and positivity. Thank you for being present when I struggled, and for pushing me when I wavered on this journey.

Table of Contents

List of Tables

List of Figures

List of Abbreviations

ADC	analog-to-digital converter
AE	adaptive equalization
AMZI	asymmetric Mach-Zehnder modulator
AOS	acousto-optic switch
ASE	amplified spontaneous emission
AWG	arrayed waveguide grating
BER	bit-error-rate
BPD	balanced photodetector
BPG	bit pattern generator
BPSK	binary phase-shift keying
CDC	colorless, directionless, contentionless
CDR	clock and data recovery
CW	continuous wave
DCF	dispersion compensating fiber
DFB	distributed feedback
DOF	degree of freedom
DOP	degree of polarization
DPSK	differential phase-shift keying
DSO	digital signal oscilloscope
DSP	digital signal processing
DWDM	dense wavelength-division multiplexing
ECL	external cavity laser
ED	error detector
EDFA	Erbium-doped fiber amplifier
EF	error-free
FEC	forward error correction
FIR	finite impulse response
FWM	four-wave mixing
G-M	Gordon-Mollenauer
HNLF	highly nonlinear fiber
HOPS	hybrid optical phase squeezer
HP	high power
i.i.d.	independent, identically distributed
ITU-T	International Telegraph Union–Telecommunication Standardization Sector
LA	limiting amplifier
LNF	low-noise-figure
LO	local oscillator
MF	matched filter
MPC	mechanical polarization controller
MZM	Mach-Zehnder interferometer

NLP	nonlinear lossless polarizer
NLPN	nonlinear phase noise
NLPS	nonlinear phase shift
NLSE	nonlinear Schrodinger equation
NOLM	nonlinear optical loop mirror
NOSP	nonlinear optical signal processing
NRZ	non-return-to-zero
OBPF	optical bandpass filter
OOK	on-off keying
OSA	optical signal analyzer
OSNR	optical signal-to-noise ratio
PA	polarization analyzer
PBS	polarization beam splitter
p.d.f.	probability density function
PDL	polarization-dependent loss
PLL	phase-locked loop
PM	polarization-maintaining
PMD	polarization mode dispersion
PRBS	pseudo-random bit sequence
PS	polarization scrambler
PSA	phase-sensitive amplifier
PSD	power spectral density
PSK	phase-shift keying
PSP	principle state of polarization
QAM	quadrature amplitude modulation
QPSK	quadrature phase-shift keying
RB	resolution bandwidth
RL	recirculating loop
ROADM	reconfigurable optical add-drop multiplexer
RT	round trip
SBS	stimulated Brillouin scattering
SBSS	SBS suppression
SNR	signal-to-noise ratio
SOP	state of polarization
SPM	self-phase modulation
SSMF	standard single-mode fiber
SVE	slowly-varying envelope
VNI	Visual Networking Index
VOA	variable optical attenuator
WSS	wavelength selective switch
XPM	cross-phase modulation
ZB	Zettabyte

Chapter 1

Introduction

1.1 Motivation

The dramatic growth of innovative internet-based advances has been enabled by the exponential growth of optical network services in our recent “Zettabyte Era”. Annual global IP traffic in 2016 was 1.2 zettabytes (ZB)/year, and in 2021 it will reach 3.3 ZB/year [1]. To put this growth rate into perspective, consider that the internet began to scale for global government and business use in the 1980’s. It has taken >30 years of innovation to reach the zettabyte benchmark and that annual run rate is predicted to nearly triple by 2021. According to Cisco’s annual Visual Networking Index (VNI), this growth may be categorized by 4 drivers: more connected devices, more IPv6-capable devices, faster global fixed broadband speeds, and more rich media content. The fourth, most impactful, driver includes the 15-fold growth of live internet video, the 20-fold growth of virtual reality, and the 10-fold growth of internet gaming traffic, within a short 5-year span. To accommodate for this continuous exponential growth of internet traffic, nonlinear optical signal processing (NOSP) applications enabled the flexible management and interface between different optical networks. The application space of NOSP includes wavelength conversion, equalization, correlation multiplexing/de-multiplexing, and multicasting [2]. A combination of multiple NOSP applications have been combined to realize subsystems, such as the colorless, directionless, and contentionless (CDC)

reconfigurable optical add/drop multiplexors (ROADMs) which enabled the rapid increase in the number of waves that dense wavelength division multiplexing (DWDM) could support [3].

The de-polarization of an optical signal during a long-haul fiber transmission is a well-documented phenomenon [4–9]. Certain implementations of NOSP applications have shown a dependency on the signal's input polarization, which may produce undesirable polarization-sensitive losses (PDL) across the application [10–13]. Assuming there is a desire to use a polarization-sensitive NOSP application on the signal, then it may be advantageous to re-localize a scrambled signal's state of polarization (SOP) via a nonlinear lossless polarization (NLP) technique before the NOSP. Polarization attraction (PA) is a NLP technique that has demonstrated success for pulse train [14] and OOK signals [15–19]. Proof-of-principle demonstrations need to be conducted for a scrambled phase-shift-keyed (PSK) signal before PA may be realized as a useful or practical technology. Also the robustness of PA to transmission impairments, such as accumulated amplified spontaneous emission (ASE) or nonlinearities, also needs to be evaluated. Hence, this dissertation aims to accomplish both of these benchmarks for polarization attraction to test its efficacy in a more realistic long-haul transmission experiment.

1.2 Organization of this Work

The rest of this dissertation is organized as follows: In Chapter 2, an investigation was carried out for the counter-propagating beam configuration of PA employed for a 10.7-GBaud non-return-to-zero binary-phase-shift-keyed (NRZ-BPSK) signal in a 1-km-long

highly nonlinear fiber (HNLF) by using the Kerr nonlinear cross-polarization. The efficacy of mitigating polarization-dependent loss across polarization-sensitive devices was emulated with a linear polarizer located before the receiver. The receiver sensitivity penalty at a bit-error-rate (BER) metric of 10^{-9} relative to the baseline NRZ-BPSK signal was < 0.5 dB and degree of polarization (DOP) > 90%, when polarization attraction was employed for a polarization-scrambled signal. The results confirm that PA is applicable to the BPSK format, and potentially higher cardinalities of PSK. In Chapter 3, a coherent reception investigation was carried on PA of a polarization-scrambled 10.7-GBaud NRZ-BPSK signal pre-loaded with ASE before injection into the HNLF. For PA on an ASE-loaded signal, the receiver sensitivity penalty at the G.709.1 forward error correction (FEC) threshold (with BER metric of $3.8 \cdot 10^{-3}$), was found to be ≈ 10.5 dB relative to the baseline case. After long-haul 100-GHz DWDM transmission in a recirculating loop, PA on the output signal was found to achieve approximately the same receiver sensitivity performance as the ASE-loaded case. Chapter 4 summarizes this dissertation with a discussion of the results and future work. It is concluded from these experiments that the Gordon-Mollenauer (G-M) effect, due to ASE interacting with the nonlinearity of the HNLF, dominates other impairments including those arising in the DWDM transmission. An analysis is provided within the Chapter 5 Appendix, where a specialized derivation of the G-M theory for this HNLF supports the experimental results.

Chapter 2

Polarization attraction of a 10.7-GBaud NRZ-BPSK signal in a highly nonlinear fiber

2.1 Introduction

Within a short propagation distance of several kilometers in standard fibers, the optical field experiences random polarization fluctuations induced by polarization mode dispersion (PMD) [4–6]. The fiber Kerr nonlinearity has also been found to contribute to depolarization [7–9]. Polarization-sensitive NOSP-based techniques are adversely affected by polarization fluctuations [20]. In this context, development of techniques with the capability to control and stabilize randomly polarized optical signals can facilitate the development of NOSP-based functions. The simplest solution to polarize a signal would be the use of an inline standard linear polarizer to allow 100% transmission for a single state of polarization (SOP) at the expense of other SOPs [21]. However, a signal with a scrambled polarization would experience significant amplitude fluctuations after passing through the polarizer. The resultant polarization-dependent loss (PDL) would create serious penalties when implementing NOSP-based techniques sensitive to amplitude fluctuations [22,23]. For these reasons, there has been a strong interest in developing lossless polarizers.

Historically, the first lossless polarizer used two-beam coupling within a photorefractive material [24], but the application of this device in telecommunications was limited by the

slow response time (on the order of multiple seconds) of photorefractive crystals. Nonlinear lossless polarizers (NLP)'s that utilized the ultra-fast Kerr nonlinearity within optical fibers showed a response time more applicable to telecommunications [25]. The phenomenon, termed "polarization attraction", is characterized by the re-polarization of an unpolarized signal when it interacts with a fully-polarized continuous-wave (CW) beam through a Kerr, nonlinear cross-polarization process, as discussed in Section 2.2. The first fiber-based NLP experimentally demonstrated polarization attraction in a 2-m-long, isotopic, highly nonlinear fiber (HNLF) with a counter-propagating CW pump beam [25,26]. One of the limitations of this demonstration was the need for very high-power signal/pump beams (≈45W) to obtain a sufficient nonlinear interaction. Using a longer length of fiber (≈20-km), a similar NLP with a reduced power requirement (<1 W) was later demonstrated in a Non-Zero Dispersion-Shifted Fiber [27]. Following this experiment, two more demonstrations were reported for a relatively shorter fiber span of 6.2 km and a reduced power requirement (<1.1 W) [28,29]. Simulations and studies of polarization attraction corroborated that the phenomenon could potentially occur in isotropic fibers [30], highly birefringent spun fibers [31], and randomly birefringent fibers [32,33]. The theory presented in [34] derived a general model for fiber-based NLPs, covering all three of the fiber types reported. Several more realizations of polarization attraction have been demonstrated on pulse train [14] and on-off keyed (OOK) signals [15–19]. All of the referenced practical demonstrations were conducted with fibers characterized by low PMD values (<0.05 ps/km$^{1/2}$) [27]. A low-PMD fiber was reported to support a more effective polarization attraction [28], [30], [34], [35]. The

demonstration within this report will follow suit with past successful experiments and utilize a HNLF with a low-PMD value (≈ 0.02 ps/km$^{1/2}$).

While OOK is one of the most cost-efficient modulation scheme, there are transmission advantages to using alternative modulation schemes that rely on the phase of the signal instead of its amplitude. The simplest such signal is binary phase-shift keying (BPSK). Theoretically, BPSK requires a minimum of 3 dB less optical signal-to-noise ratio (OSNR) than OOK to reach a given BER, for amplified spontaneous emission (ASE)-limited transmission [36]. Furthermore, it has been speculated that the effectiveness of polarization attraction might improve when employed for PSK modulation formats, since the nonlinear interaction would occur between the CW pump and a signal characterized by constant intensity [17]. However, a constant intensity BPSK signal is generated using a waveguide phase modulator, whereas a Mach-Zehnder modulator (MZM) was used for this report. Although an MZM can be superior in performance when properly biased and driven, it also introduces undesirable amplitude modulation. Consequently, the BPSK signal was periodic, but not constant in intensity. In this report, polarization attraction in a HNLF is experimentally demonstrated to all-optically control and stabilize the SOP of a 10-GBaudnon-return-to-zero (NRZ)-BPSK signal. In Section 2.2, the principle of operation of polarization attraction is summarized and the sensitivity to the CW pump SOP and power are emphasized. Section 2.3 is broken down into three subsections which collectively cover all the experimental results. In 2.3.1, the details of the experimental setup are discussed, then in 2.3.2 the mitigation of stimulated Brillouin scattering (SBS) is demonstrated. Finally, qualitative polarization

attraction observations are presented in in 2.3.3 along with the receiver sensitivity measurements and the chapter concludes with Section 2.4.

2.2 Principle of polarization attraction

The scheme for polarization attraction is shown in Fig. 2.1. It involves a data-bearing signal with a scrambled SOP injected into a HNLF, along with a counter-propagating, fully-polarized CW pump. The SOP of the signal at the output of the HNLF converges onto a tightly localized statistical distribution of SOPs. In this paper, the signal SOP is analyzed using Stokes parameters, displayed onto a Poincaré sphere via a commercially available polarization analyzer (PA).

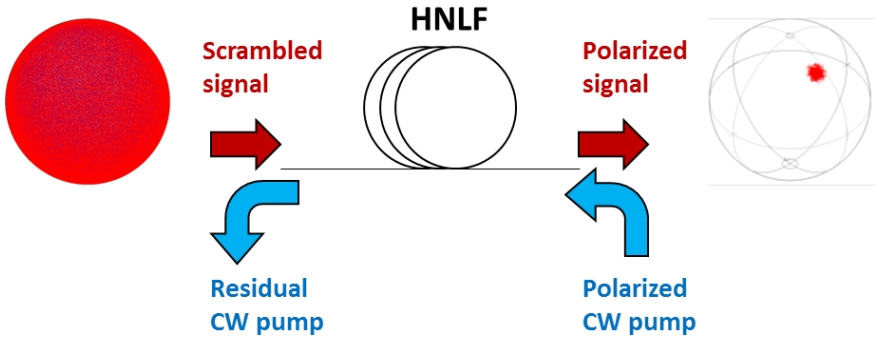

Fig. 2.1. Scheme for polarization attraction to a polarized SOP, of a signal with a scrambled SOP. PA visualizations of the signal are shown at the input and output planes of the HNLF.

The generic model for polarization attraction derived in [34] is based on four-wave mixing equations for two counter-propagating beams, and makes two assumptions regarding fiber length L. First, the birefringence orientation varies randomly over distance with a characteristic correlation length L_c, such that $L >> L_c$. Second, a statistical

parameter unique to the fiber, the differential beat length $L_B' = \left[L_B^{-1}\left(\omega_{signal}\right) - L_B^{-1}\left(\omega_{pump}\right) \right]^{-1}$ is much greater than L, in order to obtain significant re-polarization. Starting from the equations of motion for the pump and signal derived under the unidirectional and slowly-varying envelope approximations [37], coupled differential equations governed by the signal and pump Stokes vectors may be formulated [30], [34], [38]. These coupled equations imply that the signal and pump interact through a Kerr cross-polarization process, where the evolution of the SOP of the signal relies on the SOP of the pump, and vice versa. An important feature demonstrated in [34] and [17] shows that not all pump SOP's result in successful polarization. It was theoretically shown [34] that the signal is attracted to only one of two SOP's, either to that of the CW pump, or to an SOP orthogonal to that of the pump. Moreover, it was also found that the success of signal repolarization is a sensitive function of the average pump power and average signal power. Both average powers must be sufficiently high to maximize the nonlinear cross-polarization process, but the average signal power will be fixed to 0.32 W during this experiment to limit self-phase modulation (SPM)- induced spectral broadening.

The effectiveness of the polarization attraction is determined by the signal SOP distribution on the Poincaré sphere, measured by the degree of polarization (DOP) after averaging the Stokes vector [16],

$$DOP = \frac{1}{S_0^+}\sqrt{\sum_{i=1}^{3}\left\langle S_i^+ \right\rangle^2}, \qquad (1)$$

where the average of each of the Stokes parameters $\left\langle S_i^+ \right\rangle$ may be treated either as a time average or an ensemble average [29]. A DOP of unity represents perfectly polarized light

and a single SOP on the Poincaré sphere, while a DOP of zero represents polarization-scrambled light, and a full spherical coverage, within the context of this experiment. While past reports show that polarization attraction can be effective on CW beams and NRZ/RZ-OOK signals, the goal of this demonstration was to achieve polarization attraction for a NRZ-BPSK signal with a scrambled SOP and to establish whether additional impairments (beyond those for OOK) may affect the performance of a phase-shift-keyed signal.

2.3 Experimental results

2.3.1 Experimental Setup

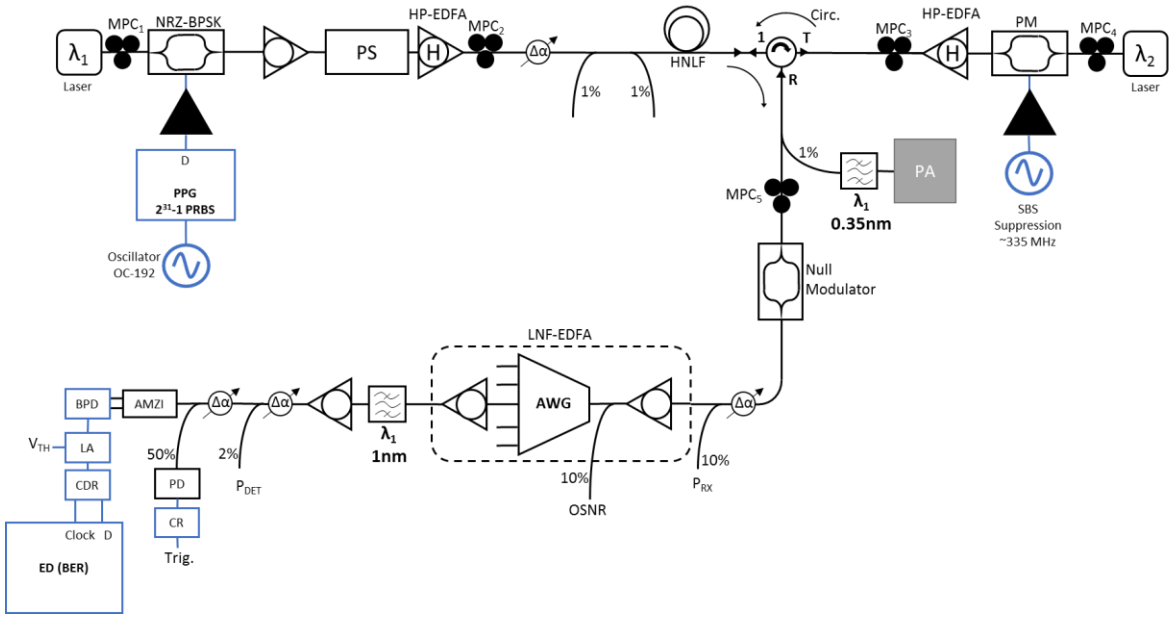

Fig. 2.2. Experimental setup for polarization attraction of a NRZ-BPSK signal. Each split in the optical path followed by a percentage indicates the presence of an optical coupler. (PPG: pulse pattern generator, PRBS: pseudo-random bit-sequence, PM: phase

modulator, MPC: mechanical polarization controller, SBS: Stimulated Brillouin Scattering, Circ: circulator, $\Delta\alpha$: variable optical attenuator, PS: polarization scrambler, HP-EDFA: high power erbium-doped fiber amplifier, LNF-EDFA: low-noise-figure EDFA, HNLF: highly nonlinear fiber, AWG: arrayed waveguide grating, AMZI: asymmetric Mach–Zehnder interferometer, PD: photo-detector, BPD: balanced PD, LA: limiting amplifier, V_{TH}: threshold voltage, CDR: clock/data recovery module, CR: clock recovery module, ED: error-detector, OSNR: optical signal-to-noise ratio measurement, Trig.: Trigger for sampling oscilloscope, P_{RX}: received power, P_{DET}: detected power).

The experimental setup for polarization attraction of a NRZ-BPSK signal is shown in Fig. 2.2. The NRZ-BPSK signal is a 10-GBaud 2^{31}-1 pseudo-random bit sequence (PRBS) centered around 1545.3 nm and may be polarized (scrambled) by turning off (on) the polarization scrambler (PS). The signal is generated by biasing a MZM at its transmission null and driving it at twice its V_π-voltage. The selection of the signal wavelength was motivated by the use of a 100-GHz channel-spaced arrayed waveguide grating (AWG) in the receiver chain. The scrambling speed of the PS was ≈ 12 kHz. The CW pump laser is centered at 1547.5 nm and phase modulated (PM) at ≈ 335 MHz in order to suppress SBS, as discussed in Section 2.3.2. As will be seen later, the wavelength of the CW pump is not critical for the fiber used. Mechanical polarization controllers were used between the lasers and the modulators due to the dearth of polarization-maintaining components. The launch powers for the signal and pump are approximately 0.32 W and 1.4 W, respectively, and their selection is discussed in the following section. The 1-km standard HNLF manufactured by OFS with part number "HNLF-ST-1000-1-1-z0", exhibits a nonlinear coefficient of $\gamma \approx 11 W^{-1}\cdot km^{-1}$, a dispersion coefficient of $D \approx -0.16 ps\cdot nm^{-1}\cdot km^{-1}$, and a PMD parameter of ≈ 0.02 ps/km$^{1/2}$. The circulator allows nearly 100% coupling of

the CW pump into the HNLF, simultaneously with nearly 100% coupling of the HNLF output to the receiver. The PA monitors the signal SOP and DOP beyond an optical bandpass filter (OBPF) tuned to the signal wavelength. The null modulator is an un-driven conventional *x*-cut $LiNbO_3$ modulator (PDL ≈ 25.4 dB) and behaves as a polarizer due to the presence of a polarizing element at its input plane, and therefore emulates the behavior of a polarization-sensitive device. The received signal is monitored at the output of the null modulator to test the quality of the polarization attraction. The initial pump SOP has a significant impact on the output signal's DOP [34], [17], where some pump SOP's produce a DOP >90% whereas others may produce a DOP comparable to that of partially polarized light (<20%).Therefore, the pump SOP is adjusted using a mechanical polarization controller (MPC_3) after its high power (HP)- Erbium-doped fiber amplifier (EDFA) to optimize the polarization attraction effect. After the signal SOP had undergone polarization attraction, the new signal SOP must be adjusted via MPC_5 directly before the null modulator to ensure maximum transmission. The NRZ-BPSK signal is evaluated as a NRZ- differential-PSK (DPSK) signal using a differential, direct-detection receiver. The DPSK receiver consists of a dual-stage, high-gain, low-noise-figure (LNF)- EDFA utilizing a 100 GHz AWG with a Gaussian passband -3-dB-bandwidth of 0.45 nm. The AWG is used in the receiver chain so that this same receiver could be used with a DWDM system in a future experiment. The chosen inter-stage filter for the elimination of out-of-band ASE is a Gaussian filter with a -3dB-bandwidth of 1 nm. The rest of this receiver consists of a 1-bit-delay asymmetric Mach-Zehnder interferometer (AMZI), a balanced photo-detector (BPD), a limiting amplifier (LA), a clock/data recovery module (CDR), and an error detector (ED). During receiver

sensitivity measurements, the OSNR is varied by varying the attenuation before the LNF-EDFA, and the detected power is kept constant at approximately 0 dBm by adjusting the attenuation after the LNF-EDFA.

2.3.2 Suppression of stimulated Brillouin scattering

Stimulated Brillouin scattering (SBS) is a nonlinear inelastic scattering process that originates from a physical phenomenon called electrostriction [39,40]. The efficacy of the scattering process is dependent on the signal's power and linewidth. The undesirable effects of SBS are easily observed from the input-output characteristic of the CW pump wave propagating through the HNLF [41]. The result in Fig.2.3 (red diamonds) shows that the output power begins to saturate at a threshold input power level of approximately 16 dBm (0.04 W) and the output power is never able to exceed 19 dBm. The SBS threshold may be generally explained as the threshold of input power where the Stokes wave power begins to increase rapidly and to approach the input signal power [39], [42].

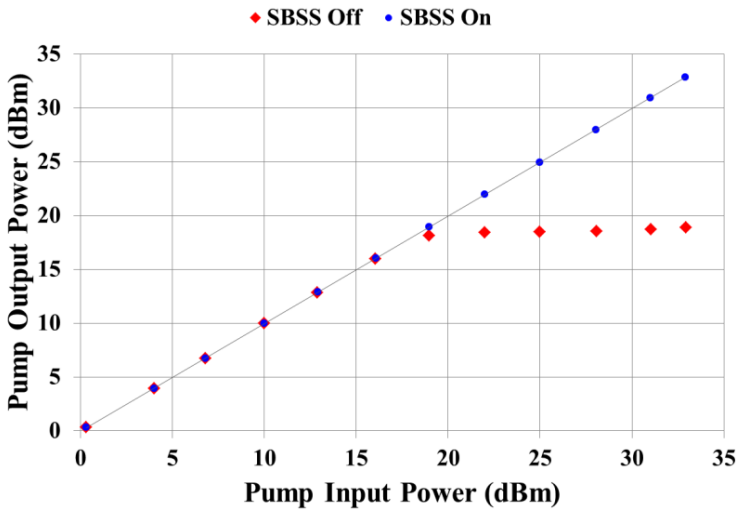

Fig. 2.3. Input-output characteristic of the CW pump wave propagating in the HNLF with SBS suppression off (red diamonds), and SBS suppression on (blue circles). A linear least-squares fit (black line) may be plotted for the latter, with a coefficient of determination $R^2 = 0.9999$.

As discussed in Section 2.2, a high CW pump power is necessary to induce strong polarization attraction. In this context, it is desirable to increase the SBS threshold of the CW pump in the fiber, which can be achieved by using external phase modulation [43]. This leads to pump linewidth broadening and a significant rise in SBS threshold [44]. The optimal phase modulation frequency was found by keeping the pump input power constant while varying the frequency from DC to 500 MHz to find a maximum pump output power. When the CW pump is phase modulated at a frequency of ≈ 335 MHz, SBS is sufficiently suppressed in the HNLF so that the output power for the pump is maximized, as shown in Fig. 2.3 (blue circles). With SBS suppression (SBSS) turned on, the CW pump may reach an output power > 31.76 dBm (1.5 W), which is high enough to

meet the 1.4 W CW pump requirement in the polarization attraction experiment demonstrated.

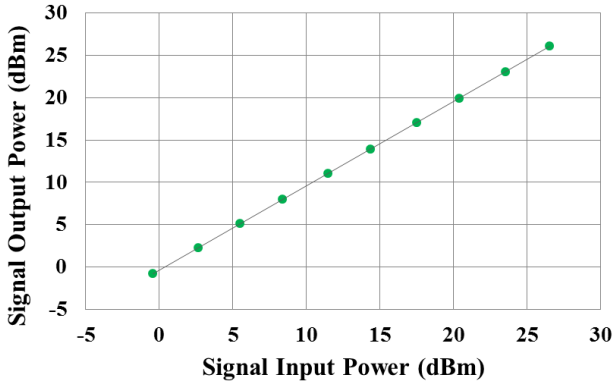

Fig. 2.4. Input-output characteristic of the NRZ-BPSK signal propagating in the HNLF, where no SBS suppression was required. A linear least-squares fit (black line) may be plotted with a coefficient of determination $R^2 = 0.9999$.

The same input-output characteristic measurements may also be applied to the NRZ-BPSK signal, to look for an indication of an SBS threshold. The plot in Fig. 2.4 shows that no significant SBS exists for the NRZ-BPSK signal propagating in the HNLF for input power $\leq$ 26.53 dBm (0.45 W) and for 2^{31}-1 PRBS, and therefore no SBSS was required for the signal.

2.3.3. Demonstration of polarization attraction of a NRZ-BPSK signal

To maximize the effect of polarization attraction as described in Section 2.2, the CW pump average power and SOP are optimized to achieve the highest signal DOP at the HNLF output. The signal DOP increases almost linearly with respect to the pump average power until a saturation pump power is reached, as demonstrated in [16]. The optimal pump average power in this demonstration is approximately 1.4 W (for a signal average

power of 0.32 W) since no significant improvement to the output signal DOP occurs for pump power >1.4 W. This is confirmed by Fig. 2.5. It was also confirmed that no detectable signal power depletion occurred at the output when the pump power was increased to its optimal level. The pump SOP is also adjusted via a MPC_3 to maximize the signal DOP at the HNLF output, since some pump polarizations perform attraction better than others [34]. Under these conditions, a signal DOP ≈ 91% was achieved, as shown in Fig. 2.6. An additional MPC_5 is required after the HNLF to adjust the attracted signal SOP for maximum transmission through the null modulator. Receiver sensitivity measurements were taken at the output of the null modulator. The signal launch power of 0.32 W was selected since this power results in the lowest BER for a given OSNR.

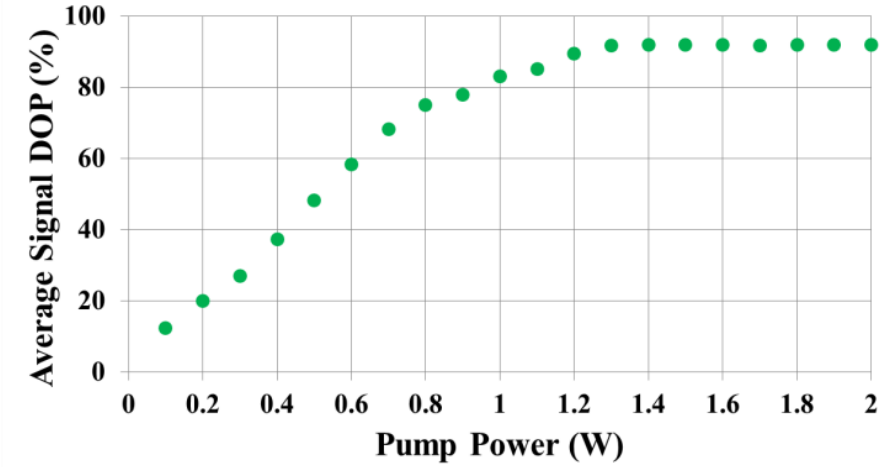

Fig. 2.5. Output signal DOP as a function of CW pump power, demonstrating that DOP saturation is achieved at ≈ 1.3 W.

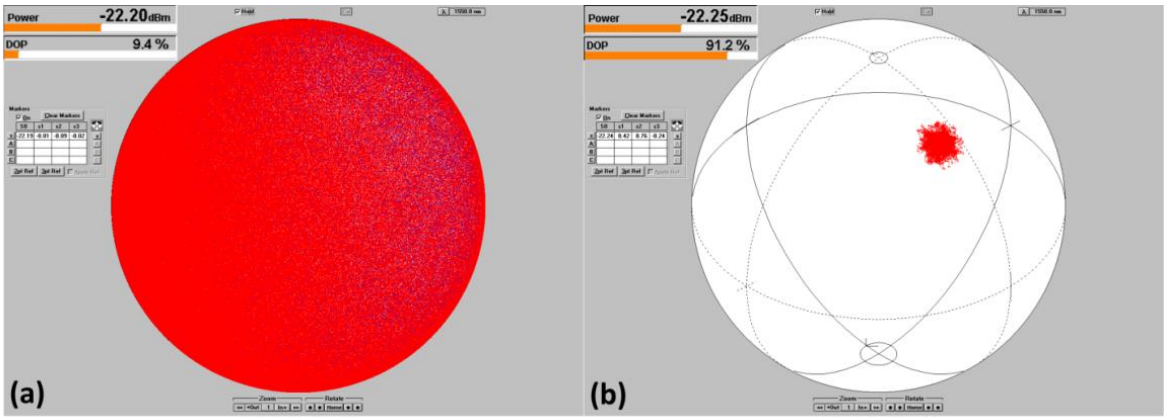

Fig. 2.6. Polarization analyzer visualizations of the scrambled NRZ-BPSK signal's state of polarization are captured with an average over 100 measurements. Figures are taken at the output of the HNLF with (a) CW pump off, DOP ≈ 9.4%, and (b) with CW pump on, DOP ≈ 91.2%.

It was confirmed that polarization attraction was fairly independent of the pump wavelength in the HNLF, over the entire International Telegraph Union–Telecommunication Standardization Sector (ITU-T) C-band shown in Fig. 2.7. The result was achieved by keeping the signal wavelength fixed, while varying the pump wavelength, and subsequently re-assessing signal DOP. This indicates that the differential inverse beat length L_B', a statistical parameter for the HNLF, is apparently weakly dependent on wavelength. The DOP roll-off in Fig. 2.7 occurs for wavelengths $\lambda < 1532$ nm and $\lambda > 1564$ nm as a consequence of the spectral limitations of the EDFA gain used for the pump in the setup.

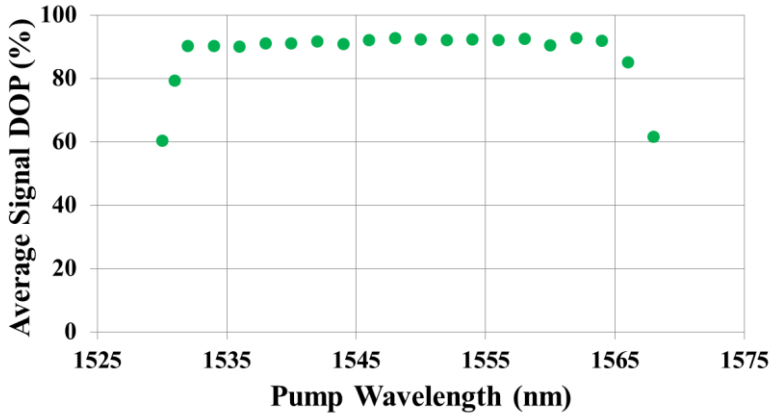

Fig. 2.7. Polarization attracted signal DOP as a function of CW pump wavelength. The signal wavelength was held fixed at 1545.3nm.

Spectra captured at different locations in the experimental setup at a resolution bandwidth (RB) = 0.01 nm are shown in Fig. 2.8. The top row shows the baseline spectra of the signal centered at 1545.3nm (red) and pump centered at 1547.5nm (blue) before they are launched into the HNLF. The spectra in the second row of Fig. 2.8 are the spectra of the signal and pump after simultaneous propagation in the HNLF. The signal experiences spectral broadening due to SPM, but the broadening is confined to spectral components > 20 dB below the spectral peak, as would be the case for super-Gaussian pulses. The AWG filter profile (black) is plotted in the third row, and the detected signal (green) is plotted on the bottom row. The -3-dB-bandwidth of the detected signal is unchanged from the unfiltered HNLF output, since the AWG filter -3-dB-bandwidth is 0.45 nm and broad enough to prevent any excessive filtering penalty. Any differences between the baseline and detected signal spectra occur > 20 dB below the spectral peak.

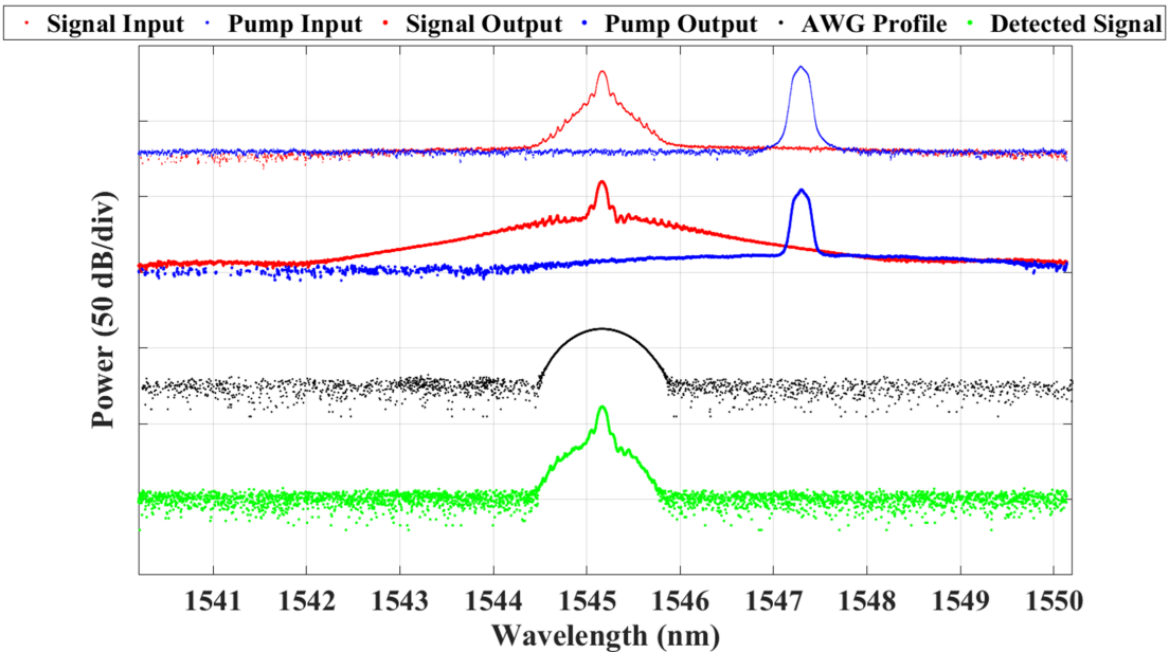

Fig. 2.8. Power Spectra captured at a resolution bandwidth of 0.01 nm for the signal (red) and pump (blue) before injection into the HNLF (top row), the signal and pump after propagating the HNLF (second row), the AWG filter profile (black, third row), and the detected signal (green, bottom row).

Qualitative comparisons of the NRZ-BPSK signal eye-diagrams captured under various conditions are shown in Fig. 2.9. The signal in all four eye-diagrams has been polarization scrambled at the transmitter. The CW pump is only turned on in the last eye-diagram, and all eye-diagrams are viewed after the AMZI, which translates phase information into amplitude. Fig. 2.9(a) shows the baseline scrambled NRZ-BPSK signal. The signal appears to experience some slight compression after propagating through the HNLF in Fig. 2.9(b) due to SPM-induced phase shifts during symbol transitions. For a constant-amplitude BPSK signal, SPM phase shifts would theoretically be cancelled out in differential detection. The signal in this report has periodic amplitude dips during

symbol transitions due to MZM signal generation and finite-bandwidth baseband components. The eye-diagram opening in Fig. 2.9(c) is filled after passing through the null modulator, which contains a polarizer, resulting in error detector synchronization loss. These fluctuations are mitigated when polarization attraction is employed in Fig. 2.9(d), when the CW pump is turned on and each MPC adjusted for optimal performance.

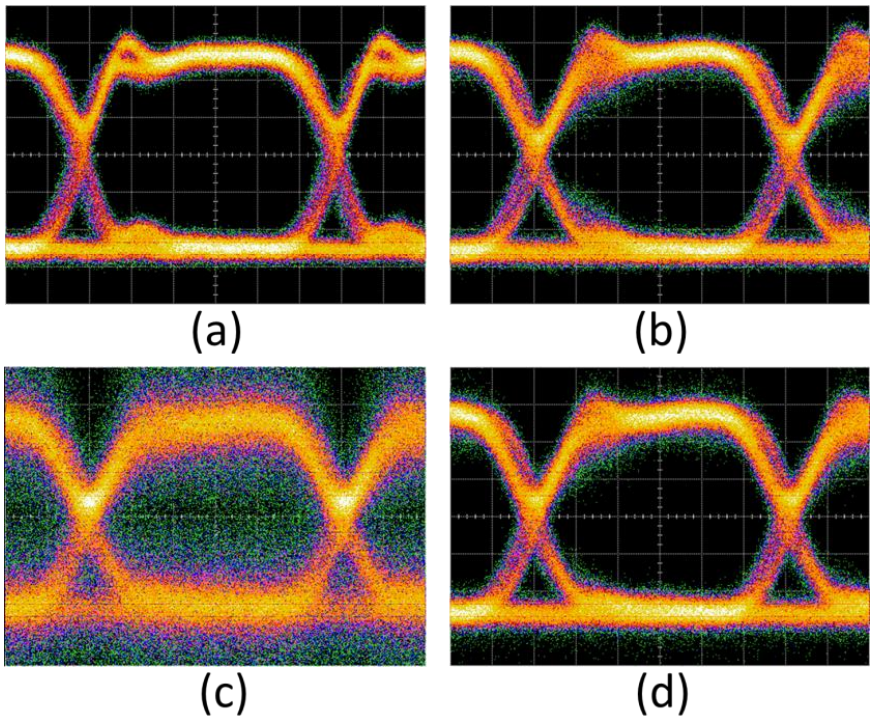

Fig. 2.9. Polarization scrambled NRZ-BPSK signal eye-diagrams captured in color-grade infinite persistence mode using a sampling oscilloscope module with a 50 GHz bandwidth and a 50 GHz balanced photo-detector at an OSNR > 40 dB/0.1nm. Fig. 2.9(a) displays the signal captured for the baseline (HNLF bypassed), Fig. 2.9(b) displays the signal after propagating through the HNLF, Fig. 2.9(c) displays the signal at the output of the null modulator where polarization fluctuations are translated into PDL, and Fig. 2.9(d) displays the polarization-attracted signal at the output of the null modulator, when the eye-diagram opening is cleared of errors, using polarization attraction.

For the baseline eye-diagram shown in Fig. 2.9(a), essentially error free detection is possible for an OSNR > 11 dB/0.1 nm as demonstrated in Fig. 2.10. The polarization attraction case shown in Fig. 2.9(d) demonstrates a penalty < 0.5 dB at a BER of 10^{-9}, relative to the baseline case, shown in Fig. 2.10. The theoretical receiver sensitivity for DPSK direct-detection in ASE-limited transmission systems, with a matched optical filter and no electrical post-filtering is also plotted in Fig. 2.10, and defined as [45]:

$$BER = \left(\frac{1}{2} + \frac{1}{4} \frac{\Delta B}{R} OSNR \right) \cdot e^{-2 \frac{\Delta B}{R} OSNR}, \qquad (2)$$

where $\Delta B / R$ represents the ratio of OSNR resolution bandwidth to bit-rate.

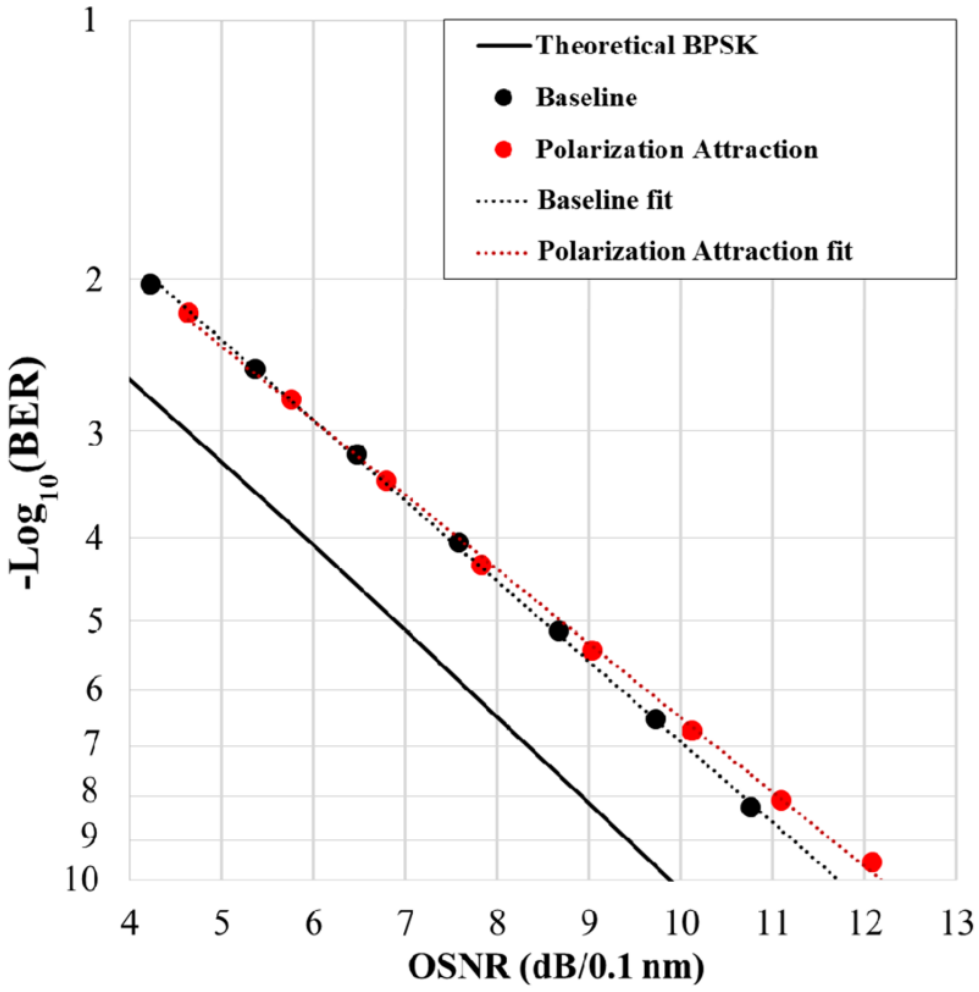

Fig. 2.10. Receiver sensitivity measurements for NRZ-BPSK when the signal was scrambled, polarization attraction was employed, and the signal was observed at the output of the null modulator (red circles), compared against the baseline (black circles). When the CW pump was off, synchronization loss resulted at the error detector. An exponential least-squares fit may be applied to the polarization attraction data points with R^2 = 0.999 (dotted red line), and another exponential least-squares fit may be applied to the baseline data points with R^2 = 0.9995 (dotted black line). The theoretical receiver sensitivity for DPSK direct-detection in ASE-limited transmission systems, with a matched optical filter and no electrical post-filtering is also plotted (solid black line).

2.4 Summary

For the first time, a 10-GBaud NRZ-BPSK signal polarization attraction experiment was successfully demonstrated via a counter-propagating configuration, in a 1-km-long HNLF. This was achieved by adjusting the CW pump's average power and its SOP in order to maximize the interactions within the Kerr cross-polarization process. SBS induced by the CW pump was suppressed via phase modulation at ≈ 335MHz in order to attain the optimal pump average power. Compared to the back-to-back baseline, the 10^{-9}–BER receiver sensitivity penalty was < 0.5 dB, with the penalty most likely due to the signal's incomplete polarization attraction (≈ 91% DOP instead of 100% DOP), and therefore undesired amplitude modulation due to passage through the null modulator (polarizer). The experiment confirms that polarization attraction with counter-propagating beams is practically insensitive to modulation format. The choice of nonlinear fiber required for efficacious polarization attraction without incurring undesirable (possibly nonlinear) impairments has been analyzed by Barozzi and Vannucci [46].

Polarization attraction should be amenable to quadrature phase-shift-keying (QPSK) (which is comprised of two BPSK signals in quadrature), although the penalty due to incomplete polarization attraction will be higher due to the reduced inter-symbol distance for QPSK, relative to BPSK. For 100 Gb/s applications and irrespective of format, polarization attraction would not be possible without some sort of polarization diversity since standard 100 Gb/s employs polarization multiplexing. The difficulty arises due to cross-polarization modulation, which plagues both deterministic and randomly-

varying birefringent nonlinear fibers. Furthermore, this experiment may be extended to an alternate “omnipolarization” configuration in polarization mode [47], where a signal self-organizes its own SOP, without the need for additional controlling beams, resulting in a simpler implementation. However, the response time could be slower by a factor of 10 compared to that attainable with the counter-propagating configuration.

Chapter 3

Evaluation of the robustness of polarization attraction for 10.7-GBaud NRZ-BPSK after long-haul DWDM transmission

3.1 Introduction

As previously mentioned in Chapter 1, PA has previously been demonstrated on an optical pulse train [14] and on-off keyed (OOK) signals [15–19]. In Chapter 2, polarization-scrambled NRZ-BPSK signal was stabilized for the first time in a HNLF to demonstrate that polarization attraction is feasible for phase-shift keying [48]. One commonality between all of these PA experiments is that they were conducted in back-to-back configurations, where the scrambled signal inbound to the nonlinear fiber had an optical signal-to-noise-ratio (OSNR) > 45 dB/0.1nm and the receiver was limited by amplified spontaneous emission (ASE). To the extent of the authors' knowledge, polarization attraction has yet to be tested on a signal suffering transmission impairments, arising due to the interaction of dispersion, nonlinearity, PMD, and ASE.

The growth of ASE in transmission and its impact on system performance have been previously reported [49]. The interaction of ASE with nonlinearity leads to the Gordon-Mollenauer (G-M) effect for PSK signals [50], in which ASE-induced amplitude fluctuations are converted to phase fluctuations via self-phase modulation (SPM) and/or cross-phase modulation (XPM) during propagation. The quadrature amplitude modulation (QAM) format is also susceptible to the G-M effect, due to its use of the optical carrier phase. It has been reported that the G-M effect can result in a significant

BER penalty [51–53]. The nonlinearity in the PA medium is critical for the efficacy of the cross-polarization processes over a short fiber length [34], but it may also intensify the G-M effect for a signal corrupted by ASE. This report demonstrates that when the signal accumulates ASE, either during long-haul transmission or artificially in the transmitter, the resulting G-M effect within the attraction medium can diminish the efficacy of PA.

For the first time, the demonstration of PA on a polarization-scrambled and single-polarization 10.7-GBaud NRZ-BPSK signal is evaluated with an optical coherent receiver to determine the robustness of polarization attraction to transmission impairments. In the first demonstration, polarization attraction is studied on an ASE-loaded 10.7-GBaud NRZ-BPSK signal. The purpose of this preliminary experiment is to study the impact of ASE on PA. The second demonstration utilizes a 100-GHz DWDM channel plan transmitted > 6,000 km over a dispersion managed SMF-28 recirculating loop. After transmission, the central NRZ-BPSK channel is isolated via an arrayed waveguide grating (AWG), followed by PA. Section 3.2 gives an overview of the effectiveness of PA on polarization-scrambled signals after fiber transmission. In Section 3.3, the results of each experiment are presented and details the penalties associated with OSNR degradation before and after PA, recirculating loop transmission optimization, and the results of PA post-transmission. A summary of the results and the conclusions are found in Section 3.4.

3.2 Overview of experiments

The block diagram for the first experiment is shown in Fig. 3.1. The output of a single-channel 10.7-GBaud NRZ-BPSK transmitter was followed by the addition of ASE, injection into the polarization attraction module [48], and evaluation in a 33-GHz, 40-GS/s coherent receiver. The purpose of this preliminary experiment was to evaluate the coherent reception of the polarization attraction, for an ASE-loaded polarization-scrambled NRZ-BPSK signal. It is assumed for this report that a minimum possible attraction characterized by a DOP > 0.9, is

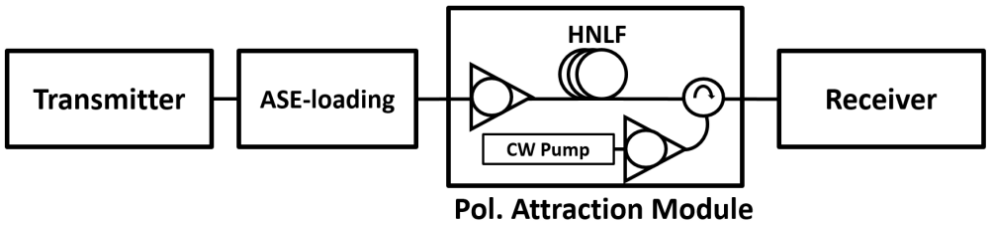

Fig. 3.1. Block diagram for the first experiment, where polarization attraction is attempted for a signal, ASE-loaded after the transmitter. The polarization attraction module was described in [29]. (ASE: amplified spontaneous emission, HNLF: highly nonlinear fiber, CW: continuous-wave).

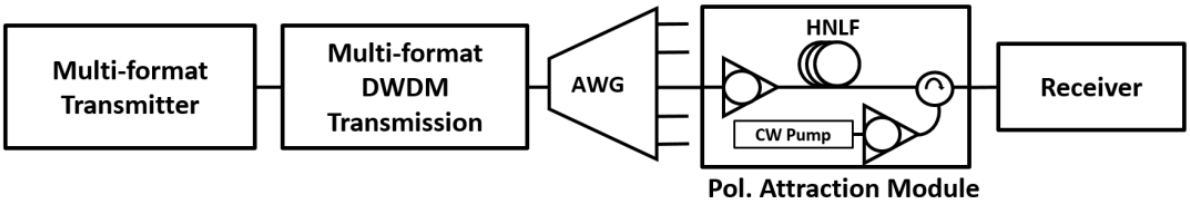

Fig. 3.2. Block diagram for the second experiment, where polarization attraction was attempted post-transmission. The Gaussian passband -3-dB-bandwidth of the 100-GHz AWG was ≈ 0.45 nm. (DWDM: dense wavelength-division multiplexing, AWG: arrayed waveguide grating, HNLF: highly nonlinear fiber, CW: continuous-wave).

necessary to mitigate penalties for some arbitrary polarization-sensitive NOSP device. It was found that a signal average launch power of 0.32 W into the HNLF was sufficient to achieve a DOP > 0.9, which required an average pump power of 1.4 W [48]. In the second experiment, polarization attraction was carried out on the NRZ-BPSK signal post-transmission in a recirculating loop (RL). Changes to the experimental block diagram in Fig. 3.2 included upgrading the single-channel transmitter to a multi-format DWDM transmitter and replacing the ASE-loading module with recirculating loop (RL) transmission. ASE-loaded back-to-back transmission can be considered to be the best-case transmission scenario, in the absence of dispersion, nonlinearity, and polarization-mode dispersion (PMD).

In the laboratory, a RL transmission system is utilized to emulate straight-line (SL) transmission, due to constraints on transmission equipment. Unlike SL-transmission, the RL is highly periodic, resulting in some impairments unique to a given RL, such as sideband instability. Other serious RL artifacts are governed by polarization effects. For PMD, the channel's state-of-polarization (SOP) can be periodically aligned with a principal state of polarization (PSP), leading to little distortion upon reception. However, it is also possible for the channel to be periodically launched between the two PSPs, leading to maximum pulse distortion over long-haul distances. It was also found that when the PDL per round-trip (RT) was minimized to ensure that the PMD was the dominant effect, the PMD grew linearly with distance, instead of with the square root of distance (as would be the case for SL-transmission.) This was due to the fact the PMD vector for one RT can be parallel (anti-parallel) to the vector for the following RT, resulting in DGD addition (cancellation) [54]. The probability density function for the RL

DGD is thus non-Maxwellian, unlike that for SL-transmission. Moreover, when PDL/RT is significant, the RL fiber realization may be such that the signal SOP is periodically aligned with the PDL low-loss axis (high-loss axis) leading to significant enhancement (degradation) of the received signal OSNR, for long-haul transmission [56]. These problems can all be significantly alleviated, rendering RL behavior closer to that of SL-transmission, by employing polarization scrambling to break the periodicity of the loop. In a later section, it will be shown that BER is optimized at a certain scrambling speed for the RL used.

The following section reports all significant experimental results and is separated into three sections. In Section 3.3.1, the results of the ASE-loaded polarization attraction experiment are presented. Section 3.3.2 reviews all the experiments performed to characterize and optimize the RL performance without polarization attraction. Section 3.3.3 presents the results of polarization attraction post-transmission.

3.3 Experiments and analyses

3.3.1 ASE-loaded polarization attraction experiment

Fig. 3.3 shows the setup used to test PA on a NRZ-BPSK signal with an artificially lowered OSNR. The transmitted signal is a 10.7-GBaud 2^{15}-1 pseudo-random bit sequence (PRBS) NRZ-BPSK signal centered at 1547.715 nm. It also served as the probe in a PA subsystem. The transmitter consisted of an external cavity laser (ECL) which was modulated by a Lithium Niobate Mach-Zehnder modulator (MZM). The MZM was biased at its transmission null and driven by a pattern generator via an RF-amplifier at

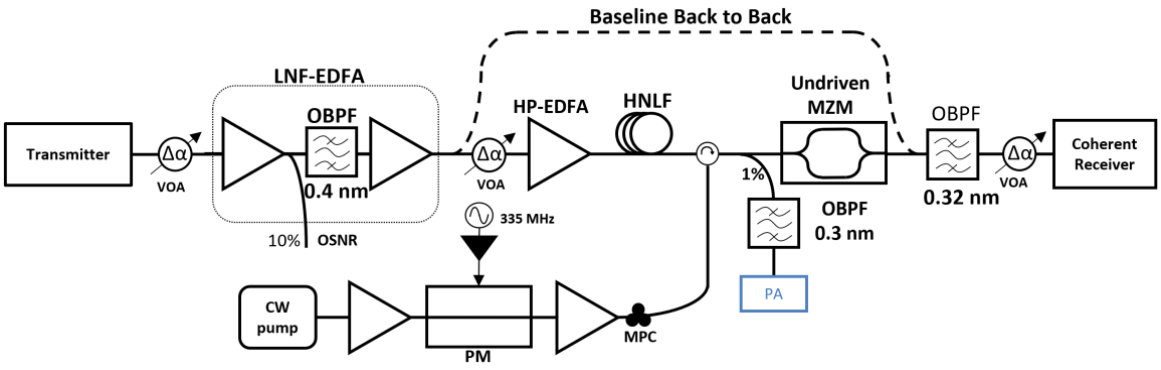

Fig. 3.3. Experimental setup for the observation of polarization attraction by propagating a scrambled ASE-loaded 10.7 GBaud NRZ-BPSK signal through a HNLF. The counter-propagating CW laser enabled polarization attraction, when required (OBPF: optical band-pass filter, MPC: mechanical polarization controller, Circ: circulator, $_{\Delta\alpha}$: variable optical attenuator (VOA), LNF-EDFA: low-noise-figure EDFA, HP-EDFA: high-power EDFA, HNLF: highly nonlinear fiber, OSNR: optical signal-to-noise ratio measurement, PA: polarization analyzer).

twice its V_π-voltage and followed by the polarization scrambler with a maximum speed of ≈ 12 kHz. The linewidth of the ECL was ≈ 65 kHz. After the transmitter, the signal could be attenuated and re-amplified by the LNF-EDFA to reduce OSNR, or it could bypass this section to allow PA at highest available OSNR. When PA was required, a CW pump laser centered at 1549.92 nm, was injected backward into the HNLF using a circulator, and was phase-modulated (PM) at ≈ 335 MHz in order to suppress SBS. The wavelength of the pump was not crucial to the efficacy of PA and a pump-probe detuning of ≈ 2 nm was selected as was the case in [48]. The respective launch powers for the signal and pump were approximately 0.32 W and 1.4 W. The 1-km-long standard HNLF exhibits a nonlinear coefficient of $\gamma \approx 11 \mathrm{W^{-1}\cdot km^{-1}}$, a loss coefficient of $\alpha \approx 0.28$ dB/km, a normal dispersion coefficient of $D \approx -0.16\ \mathrm{ps\cdot nm^{-1}\cdot km^{-1}}$, and a PMD parameter ($\sigma_T/L^{1/2}$) of ≈ 0.02

ps/km$^{1/2}$. The loss coefficient includes splice losses to standard SMF pigtails, implying that the actual propagation loss is significantly lower. The HNLF's normal dispersion precludes modulation instability [56]. Depolarization due to the total PMD was minimal due to the relatively larger coherence time of the ECL, and the low Baud-rate [4]. The polarization analyzer monitored the signal SOP and DOP. The 0.3-nm OBPF was used to isolate the signal and reject unwanted four-wave mixing (FWM) terms and out-of-band ASE. The NRZ-BPSK signal was evaluated using a 33-GHz, 40-GS/s coherent receiver. During receiver sensitivity measurements, the OSNR was degraded by the first variable optical attenuator (VOA) before the LNF-EDFA. The "ASE-loading" block in Fig. 3.1 was comprised of this VOA and the LNF-EDFA. A second VOA before the HP-EDFA was used to keep constant power into the launch EDFA. A third VOA after a 0.32-nm OBPF and before the receiver, was used to keep the power constant at 0 dBm.

The coherent receiver is shown in Fig. 3.4, and is commercially available from Keysight Technologies, Inc. The receiver consists of a polarization-diverse 90^{o}-hybrid, opto-electronic hardware, and a digital storage oscilloscope (DSO), which carries the analog-to-digital converters (ADCs) and the digital signal processing (DSP) algorithms. The 90^{o}-hybrid circuit decouples the two polarization states via a polarization-beam splitter (PBS), as well as the in-phase and the quadrature components of the signal. The four components of the signal are then mixed with a low-linewidth (~ 65 kHz) local oscillator (LO), which was always tuned to be within 0.1 GHz relative to the input signal frequency. The LO field is distributed nearly symmetrically among the two hybrids. For a polarization-scrambled, single-polarized signal, the signal's power may be in either of the *x*- or the *y*-polarization hybrid, or in both during some instants. However, the DSP

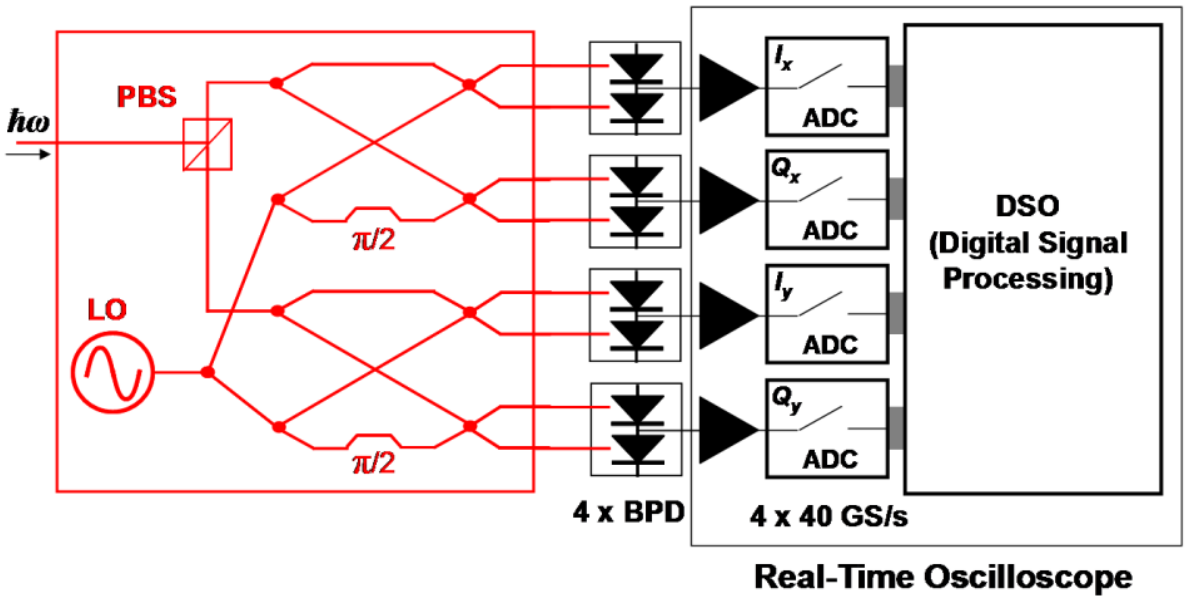

Fig. 3.4. The Keysight Technologies coherent receiver used in all the experiments. The inbound signal is represented symbolically as $\hbar\omega$.

algorithms determine whether the signal is single- or dual-polarization, based on any inter-polarization decorrelation. The decoupled four signals are then each detected in a balanced *pin*-detector, and subsequently amplified to ensure sufficient input power to the corresponding ADC. The effective bandwidth of an analog opto-electronic detection module, which includes a detector and its attendant low-noise amplifier, is ≈ 33 GHz. Each ADC sampled a signal at 40 GS/s, at more than thrice the Baud rate. The effective number of bits for an ADC is approximately 5.5 [57]. The DSO also hosts proprietary DSP algorithms that compensate for hardware imperfections, polarization recovery, carrier recovery, clock extraction, and symbol estimation. Additional algorithms include dispersion and PMD compensation and adaptive equalization, some of which were used in the transmission experiment and discussed later in this report. To expedite algorithmic convergence, a T-spaced (instead of a fractionally spaced) adaptive equalization (AE)

finite impulse response (FIR) filter was used. At least 10^6 symbols were evaluated for a given BER.

To carry out the baseline back-to-back (ASE-limited) receiver sensitivity measurement, all components in Fig. 3.3 between the LNF-EDFA and the 0.32-nm-OBPF were bypassed. The first VOA was used to attenuate the signal input to the LNF-EDFA to degrade the received OSNR. The last VOA after the OBPF was used to maintain constant the power at ≈ 0 dBm to the coherent receiver. In the receiver, only AE was additionally engaged, except in demonstrations of PA.

The G-M effect due to HNLF propagation could be observed qualitatively by the coherent receiver without PA and shown in Fig. 3.5. The VOA before the HP-EDFA in Fig. 3.3 was set to its minimum, intrinsic attenuation. Receiver AE was enabled for Fig. 3.5. All constellation diagrams in Fig. 3.5 were taken at the HNLF output, at varying HNLF launch powers, when the OSNR was 16 dB/0.1 nm. Increasing the launch power into the HNLF by a factor of four, from Fig. 3.5(a) to 3.5(d) enhanced the G-M effect and resulted in severe symbolic distortion.

For Fig. 3.6, the launch power was held constant at ≈ 0.32 W while the corresponding OSNR was varied by adjusting the VOA before the LNF-EDFA (Fig. 3.3). This launch power was found to be optimal for PA [48]. The VOA before the HP-EDFA was used to ensure a constant launch power into the HNLF. Fig. 3.6(a) and 3.6(c) show the signal before and after the HNLF when the input had the highest available OSNR. Fig. 3.6(b) and 3.6(d) show the signal before and after the HNLF when the input signal had been ASE-loaded down to an OSNR of ~16 dB/0.1 nm. The differences between Figs. 3.6(c) and 3.6(d) are ascribed to the G-M effect. Ho and Kahn [58] have noted that in the

presence of a significant nonlinearity, the detected symbols assume crescent-like densities due to the correlation of nonlinear phase rotation with the received intensity. In this case, the decision boundary becomes spiral-like, as opposed to a

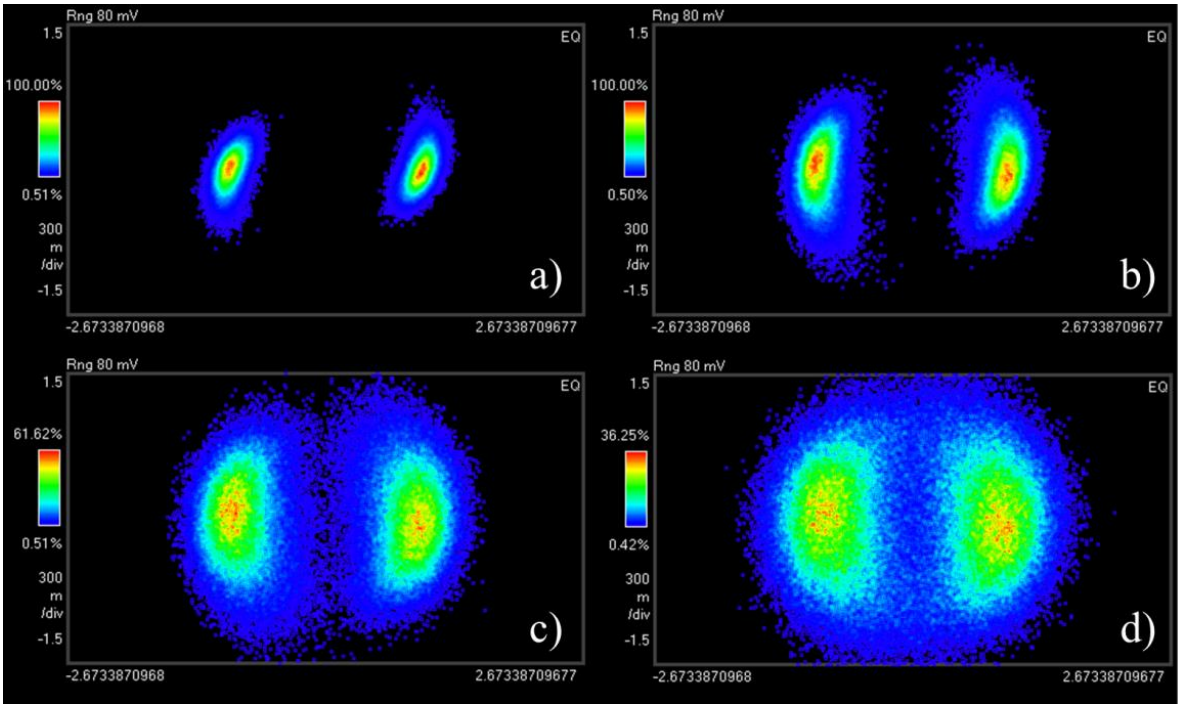

Fig. 3.5. NRZ-BPSK constellations at the output of the HNLF, captured on a coherent receiver, and as a function of average launched signal power Adaptive equalization (15-tap FIR filter) was used an optimized for each of the four cases. The signal at the HNLF input had an OSNR of ≈16 dB/0.1 nm. The received OSNR was close to 16 dB/0.1 nm and the received power was approximately 0 dBm. The average launch power into the HNLF was (a) 0.1 W, (b) 0.2 W, (c) 0.32 W, and (d) 0.4 W.

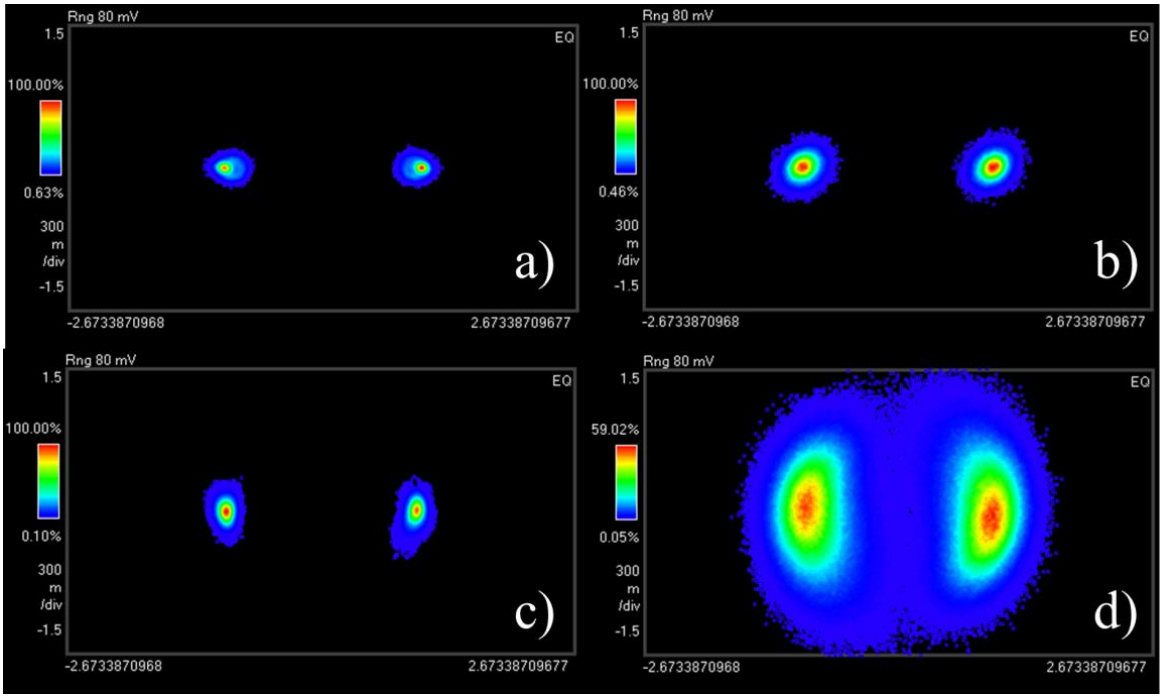

Fig. 3.6. NRZ-BPSK constellations captured on a coherent receiver, at the input (1st row), and the output (2nd row) of the HNLF, and as a function of OSNR. Adaptive equalization was used (15-tap FIR filter), and the HNLF signal launch power was 0.32 W, for all four cases (a) HNLF input at the highest OSNR, (b) HNLF input at an OSNR of 16 dB/0.1 nm, (c) HNLF output when the input was at the highest OSNR, (d) HNLF output when the input OSNR was 16 dB/0.1 nm.

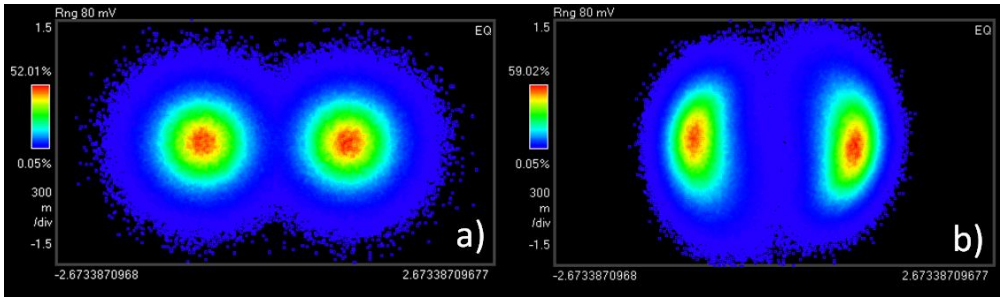

Fig. 3.7. Constellations at the FEC threshold for (a) polarization-scrambled baseline NRZ-BPSK, and (b) ASE-loaded polarization attraction of polarization-scrambled NRZ-BPSK. Adaptive equalization was engaged for both cases.

straight line normal to the real-axis that carries the two symbols as in Fig. 3.6(a) for a low launch power.

Transmitter imperfections, shown in Fig. 3.7(a), were overwhelmed by ASE as the symbols are uniformly distorted at the G.709.1 FEC BER threshold of 3.8×10^{-3}. By contrast, ASE-induced signal corruption is enhanced during PA due to nonlinear propagation in the HNLF. Fig. 3.8 summarizes receiver sensitivity measurements for the baseline and the ASE-loaded polarization attraction (PA) cases. The HNLF was bypassed to obtain the baseline receiver sensitivity, which yielded at the FEC threshold, a penalty of 4 dB maximum relative to the expected theoretical behavior,

$$\mathrm{BER} = \frac{1}{2}\mathrm{erfc}\left(\sqrt{\frac{2B_o}{R}\mathrm{OSNR}}\right) \tag{1}$$

where B_o is the resolution bandwidth (12.5 GHz), and R is the bit-rate (10.7-GBaud). The theory assumes heterodyne coherent matched-filter reception limited by ASE alone. For ASE-loaded PA, the penalty worsened to > 14.5 dB, when the signal launch power was held fixed at 0.32 W, the pump was 1.4 W, and the output DOP was ≈ 90% and constant over the entire data set. The penalty is seen to steadily increase as the OSNR is degraded (attributable to the G-M effect), as the ASE-loaded PA case diverges away from the baseline. This behavior contrasts with that of the baseline, which approximately shows no change in penalty as the OSNR is reduced. The role of the CW pump in PA was revealed by turning off the pump, which yielded a BER floor. This was due to the conversion of scrambling-induced polarization fluctuations to amplitude modulation in the undriven MZM (Fig.3.3). However, at the G.709 FEC threshold the penalty was 0.5 dB maximum. To qualitatively illustrate the efficacy of PA, the polarization recovery and AE algorithms

aboard the coherent receiver were disabled, while the inbound signal SOP was aligned with the slow axis of the PBS input in Fig. 3.4. The results are shown in Fig. 3.9, which demonstrates a symbolically compact constellation that resulted in an error-free BER. When the pump to the HNLF was turned off, and under the same conditions, the symbols became significantly diffuse and more distorted, and the corresponding BER was no longer error-free.

A receiver sensitivity experiment was carried out on HNLF propagation of a polarization-scrambled NRZ-BPSK signal, to decouple PA effects from purely nonlinear propagation in the HNLF. Its launch power was set to 0.32 W, the same as that used for the polarization attraction experiment. The CW pump was turned off. The undriven modulator was bypassed, to focus solely on the Gordon-Mollenauer effect. The results are shown in Fig. 3.10 and demonstrate an excess penalty of 0.5 dB maximum, for only HNLF propagation, relative to ASE-loaded PA. This indicates that the large penalty arising for PA is mostly attributable to the Gordon-Mollenauer effect. For all cases shown, AE was once again engaged. It was noted by Carena et al. [59] that AE forces the effective receiver filter behavior towards that of the matched filter.

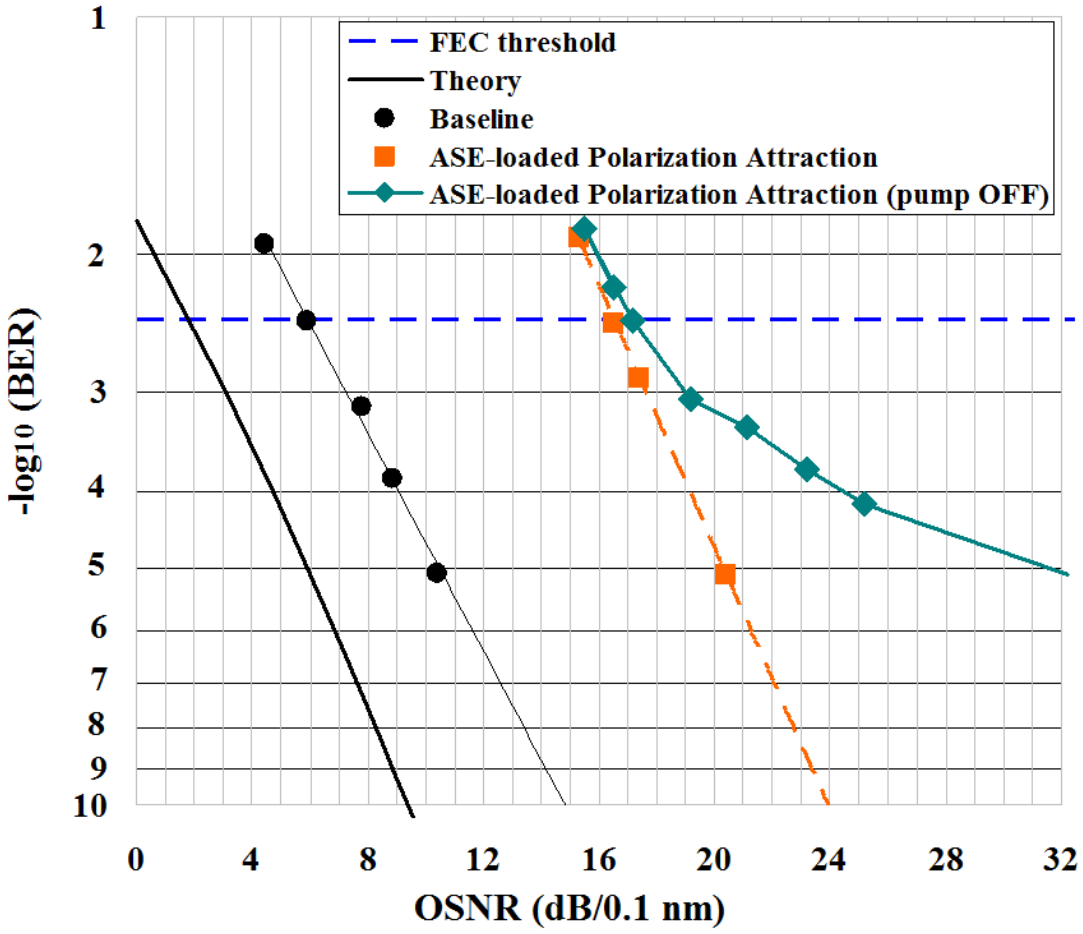

Fig. 3.8. Receiver sensitivity measurements when the signal was polarization-scrambled, ASE-loaded, and polarization attraction was employed (red squares), compared against the baseline, with the HNLF bypassed (solid circles). The "Theory" represents Eq. (1).

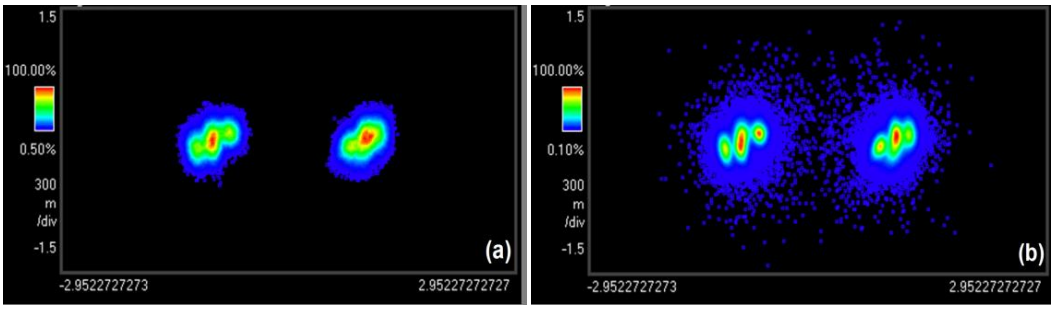

Fig. 3.9. Polarization attraction at highest OSNR, in the absence of polarization recovery, and adaptive equalization. (a) Pump on, and (b) Pump off.

Gordon and Mollenauer have derived an estimate for the nonlinear phase shift (NLPS) variance, for error-free long-haul transmission [50]. This theory is reiterated in Eq.(2), and assumes matched-filter reception. For phase modulation, they "show that there results a minimum [bit] error rate when the signal power produces a total nonlinear phase shift of approximately 1 rad." The expression may be naively applied to propagation over the 1-km HNLF, to verify the large penalty observed for PA. From Fig. 3.8 or Eq. (1), for ASE-limited, matched-filter reception, a linear OSNR of 7.7 (8.9 dB) is required for an error-free BER of 10^{-9}. If a maximum NLPS of 1 rad is additionally assumed, the nonlinear phase variance is then constrained as follows:

$$\left\langle \delta\varphi^2 \right\rangle \approx \frac{2}{3}\frac{\left\langle \varphi_{\mathrm{NL}} \right\rangle^2}{Q} = \frac{R}{3B_o}\frac{\left\langle \varphi_{\mathrm{NL}} \right\rangle^2}{\mathrm{OSNR}} \leq 0.037 \text{ rad}^2 \tag{2}$$

where Q is identical with SNR.

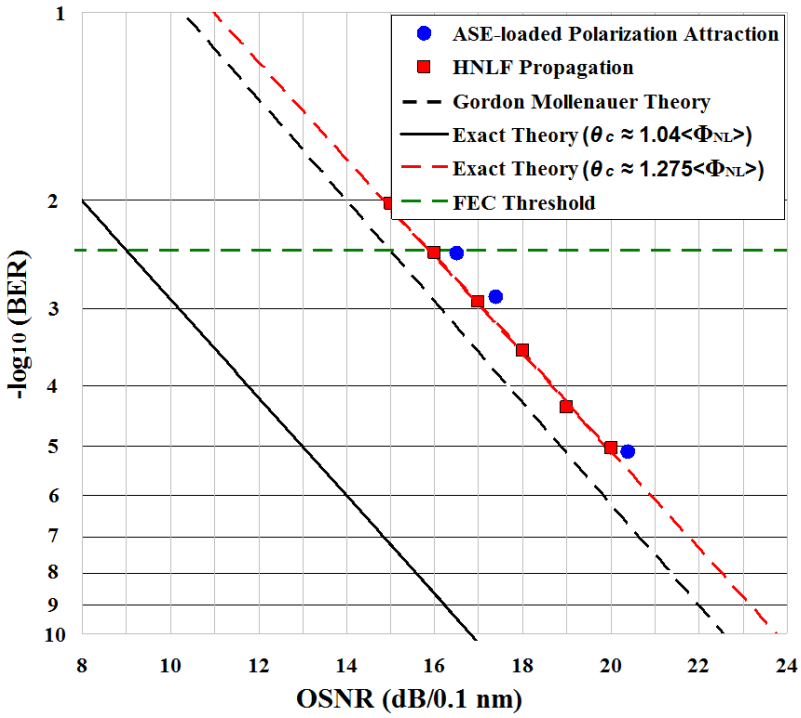

Fig. 3.10. Receiver sensitivity measurements for ASE-loaded polarization attraction (circles), compared against HNLF propagation alone (squares).Also shown is the Gordon-Mollenauer theory or Eq. (3); and the Exact Theory or Eq. (4).

It can be seen that if the NLPS φ_{NL} changes by some factor, the linear OSNR must change by the square of that factor, to keep the resultant variance at a value of no more than 0.037 rad^2 (which was obtained for a 1-rad NLPS and a linear OSNR of 7.7.) The NLPS generated in the HNLF at a launch signal power of 0.32 W was $8/9\gamma P_0 L \approx \pi$ rad, implying that the OSNR would have to be increased by π^2, which yields a linear OSNR of76 or 18.8 dB. From Fig. 3.8, the extrapolated OSNR for "HNLF Propagation" at 10^{-9}-BER is ≈ 23 dB, which is a little more than 4 dB higher than that predicted by the theory. Alternatively, it is possible to use the extrapolated OSNR in the above equation, to solve for the NLPS, which turns out to be 5.1 rad. The theory thus overestimates the experimental NLPS of π rad, by a factor of 1.6. Gordon and Mollenauer attempted an

application of their theory to a 2.5-Gb/s frequency-shift-keyed, long-haul transmission experiment [60], which yielded error-free BER at 2,200 km. It was found that the theoretical prediction of NLPS for this experimental study was inaccurate and missing a factor of 1.5 [50].

It is possible to specialize the derivation of the GM-theory to the HNLF, the details of which has been relegated to the Appendix. The condition for OSNR estimation based on the G-M theory can be summarized as follows, in general

$$\mathrm{OSNR} \geq \frac{R}{4B_o}\left(1+4\left\langle \Phi_{\mathrm{NL}} \right\rangle^2\right)\left(\mathrm{erfc}^{-1}\left(2\mathrm{BER}\right)\right)^2 . \tag{3}$$

Then for a NLPS of $\approx \pi$ rad, and 10^{-9} error-free BER, the minimum required OSNR is 156 or 21.93 dB / 0.1 nm. According to Fig. 3.8, the extrapolated OSNR required for 10^{-9} error-free BER, is $\approx$ 23 dB. Eq. (3) is thus in error by < 1.1 dB. However, extrapolation may have produced a fortuitous OSNR, leading to an erroneous conclusion for the accuracy of the Eq. (3). However, the theory can also be verified at the FEC threshold which yielded an actual BER measurement, unlike the case just examined.

For an FEC target BER of $3.8\text{x}10^{-3}$, matched-filter reception requires an OSNR of just 1.9 dB / 0.1 nm, from Fig. 3.8 or Eq. (1). Since the total power launched into the HNLF was fixed at 0.32 W irrespective of OSNR, the actual signal power is reduced at the lower OSNR's. At the FEC target BER, an OSNR of 16 dB / 0.1 nm was required in the experiment, which yields an actual signal power of 0.31 W. At this power, the NLPS generated by the HNLF is then lower, at 3.03 rad. To achieve the BER of $3.8\text{x}10^{-3}$ for a NLPS of 3.03 rad, the OSNR would have to be at least 28.8 or 14.6 dB. The error relative to the experimental OSNR of 16 dB is then 1.4 dB, slightly higher than the discrepancy at

the error-free BER. However, by using the more accurate version of Eq. (3) listed in the Appendix as Eq. (36), and solved simultaneously with Eq. (38), the estimated OSNR is estimated to be 15 dB. Once again, this is an error of 1 dB. Based on this data, "The Gordon Mollenauer Theory" was plotted on Fig. 3.10, demonstrating a uniform 1-dB penalty relative to "HNLF Propagation". The G-M theory for matched-filter reception, limited to 2 degrees of freedom, is also a good approximation in practice when the filter bandwidth is approximate the same as the signal's bandwidth. The theory is optimistic for the predicted OSNR. In the analysis, the filter bandwidth is assumed to be the optical spectrum analyzer (OSA)'s resolution bandwidth of 12.48 GHz, which is > 16% larger than the Baud-rate of 10.7-GBaud. As the filter bandwidth increases, the contributions due to the higher order noise modes become less negligible, resulting in increased variances of both linear and nonlinear phase noises. This effect is exacerbated for high launch powers and low dispersion fibers [61,62], such as the HNLF.

It is possible to use the "Exact Theory" for the BER of a BPSK signal suffering from nonlinear phase noise, and is given by

$$\mathrm{BER} = \tfrac{1}{2} - \tfrac{2}{\pi}\sum_{n=0}^{\infty}\frac{(-1)^n}{2n+1}\Re\mathrm{e}\left[\Psi^*_{\Phi_r}(2n+1)e^{-i(2n+1)\theta_c}\right] \tag{4}$$

which is dependent on the characteristic function of the received phase Ψ_{Φ_r}. This theory was also derived for matched filter reception and the expanded theoretical handling is summarized in the Appendix. The outcome is dependent on the decision angle parameter θ_c. When the mean NLPS is no more than ≈ 1.25 rad, the optimal θ_c is lower than the NLPS. For higher mean NLPS, this angle becomes larger than the NLPS. The deviation may be exacerbated for a realistic BPSK signal suffering pattern-dependence and ISI,

captured by a practical receiver. It was already found that, at the FEC threshold, baseline NRZ-BPSK BER was at least 4 dB worse than that of matched filter reception of Eq.(1). Arguably, this can result in constellation distortion unexpected by the exact theory of Eq.(4), thus shifting the optimal decision angle. It was found that θ_c had to be approximately a factor of 1.275 larger than the mean NLPS, to achieve a good agreement between Eq. (4) and the experiment (Fig. 3.10). The experimental penalty relative to the exact theory (which required a $\theta_c \approx 1.04\ \Phi_{NL}$) is approximately 7 dB at the FEC threshold, for ideal BPSK, matched-filter reception, and for the same NLPS.

3.3.2 Transmission of NRZ-BPSK in a recirculating loop

This section gives an overview of the recirculating loop (RL), including the transmitter/receiver setup, channel plan, optimal launch power, and baseline transmission receiver sensitivity performance. The NRZ-BPSK signal used in Section 3.1 now serves as the center channel in a 100-GHz DWDM transmission system. Polarization attraction (PA) on a signal output by the RL is not examined until Section 3.3.

Fig. 3.11 shows the setup used for the 100-GHz DWDM transmitter, which produced 11 de-correlated, 10.7-GBaud 2^{15}-1 PRBS NRZ-BPSK ECL channels centered around 1547.715 nm. The NRZ-BPSK signals were generated by combining all 11 channels and injecting them into a MZM biased at its transmission null and PRBS-driven at twice its V_π-voltage. The NRZ-BPSK channels were subsequently de-correlated, by demultiplexing them in an AWG, propagating them through different lengths of fiber, and multiplexing utilizing a second AWG. The fiber differential decorrelation length was at least 1 m between neighboring channels. The multi-format DWDM transmitter also

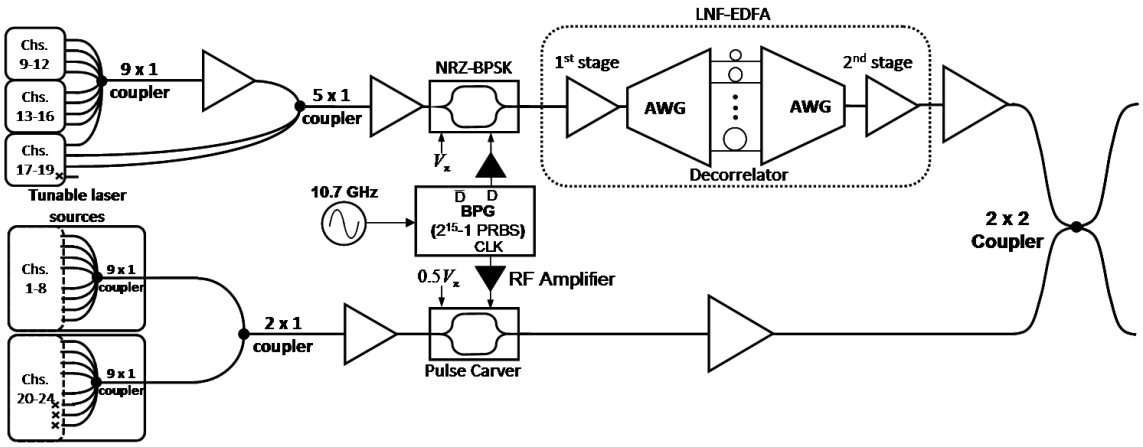

Fig. 3.11. Experimental setup for the DWDM transmitter (AWG: arrayed waveguide grating; LNF: low-noise figure; BPG: bit pattern generator).

produced 13 RZ-pulse-train signals by combining the outputs of 13 distributed feed-back (DFB) lasers into a MZM biased at quadrature and driven at its V_π-voltage by a 10.7 GHz clock. Eight of these RZ-pulse-train channels were tuned to the blue end of the 11 NRZ-BPSK channel block, whereas the remaining five were tuned to the red end of the channel block. The wavelengths of the NRZ-BPSK channels were chosen to fit within the standard ITU-T 100 GHz grid, and the wavelengths of the RZ-pulse-train channels were limited by the availability of DFB lasers.

The setup of Fig. 3.3 was used to obtain a transmission baseline for the center channel where the RL replaced the first VOA. The Transmitter was also replaced by the DWDM transmitter of Fig. 3.11. The components between the LNF-EDFA and up to the 0.32 nm filter before the receiver were bypassed. Figure 3.12 shows the setup used for the RL. The transmission line within the loop had a total length of 162.7 km, residual dispersion of 6.11 ps/nm/km, and a net PDL of 0.045 dB. Table 2.1 summarizes the characteristics of the transmission spans. A polarization scrambler was utilized to break the periodicity

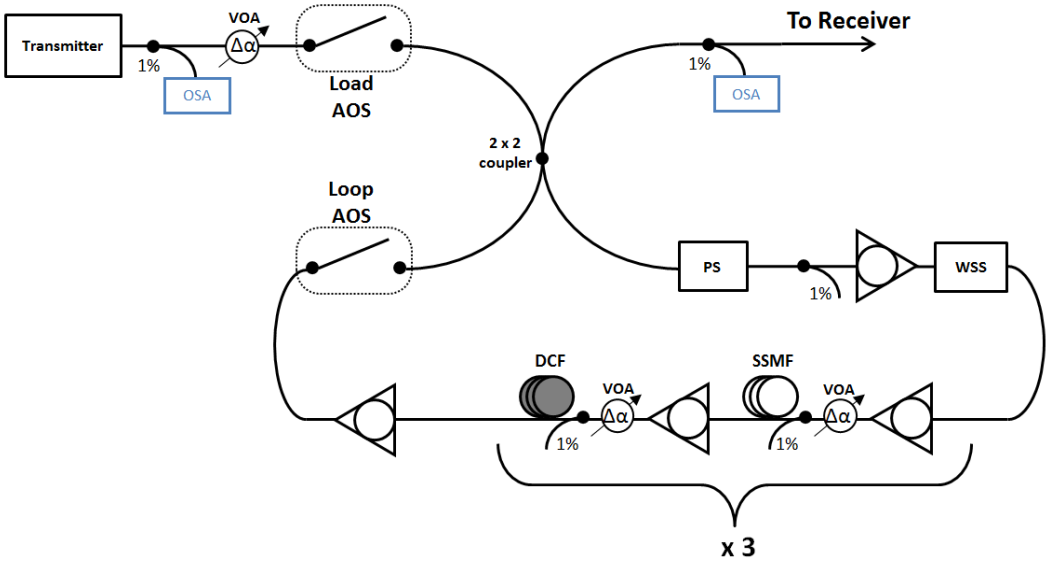

Fig. 3.12. Experimental setup for the recirculating loop. (OSA: optical spectrum analyzer, $\Delta\alpha$: variable optical attenuator (VOA), AOS: Acousto-optic switch, PS: polarization scrambler, WSS: wavelength-selective switch, SSMF: standard single-mode fiber, DCF: dispersion-compensating fiber).

Table 2.1. Recirculating loop span characteristics.

Span	L (km)	D (ps·nm^{-1}·km^{-1})	S (ps·nm^{-2}·km^{-1})	α (dB/km)	$\sigma_T/L^{1/2}$ (ps/km$^{1/2}$)
1	45.9	16.6	0.06	0.33	0.06
2	43.0	16.9	0.06	0.33	0.02
3	50.4	17.1	0.06	0.30	0.26

of the RL, thus mitigating artifacts due to PMD [54] and PDL [63]. The wavelength-selective switch (WSS) was used to correct for gain-tilt and gain ripple due to repeated amplification in the RL, which could enhance nonlinear effects during propagation. However, this correction was only carried out once per circulation and not after each

amplification stage, so that the channels were indeed launched into each span with some gain artifacts. The gain artifacts and tilt could exacerbate transmission impairments over long-haul distances. The OSA at the output of the RL was gated to monitor the spectra after each circulation for correction with the WSS. The 1% taps before each span were calibrated to monitor launch power. Launch powers could be adjusted using programmable VOAs after each EDFA. The effects of scrambling speed on received central channel Q (observed on the coherent receiver) are shown in Fig. 3.13. The optimal scrambling speed was determined to be at least 10 kHz, which was the maximum operating rate of the RL polarization scrambler. These measurements were taken at a distance of > 5,000 km and readily reproducible at further transmission distances.

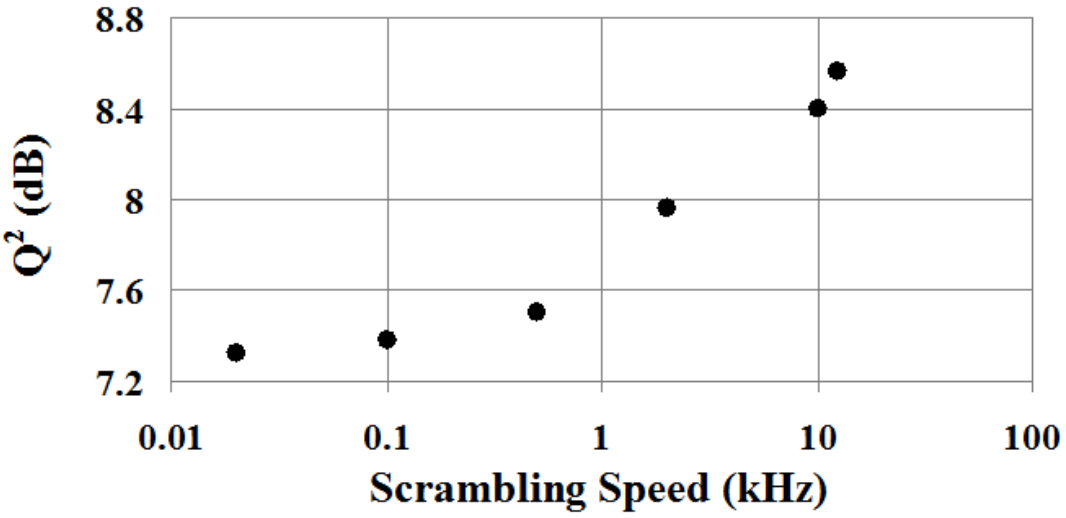

Fig. 3.13. Q^2 vs. logarithmic scrambling speed of the polarization scrambler. Q^2 values were measured after a transmission distance of > 5,000 km.

To optimize transmission, the fiber span launch power was varied while BER was measured approximately about the G.709.1 FEC threshold [64]. All BER measurements were taken for the center channel (1547.715 nm) after 7,321.5 km of transmission. The

optimal launch power was approximately -10.5 dBm per channel around the chosen FEC threshold and shown in Figure 3.14. For all measurements the dispersion compensating fiber (DCF) launch power was fixed -10 dBm per channel to ensure quasi-linear transmission. These launch powers were measured using a 1% tap before each of the standard single-mode fiber (SSMF) and DCF spools shown in Fig. 3.12, after adjustment for the loss in each tap. The AE filter was re-optimized and found to be approximately 11-symbols long (Fig. 3.15).

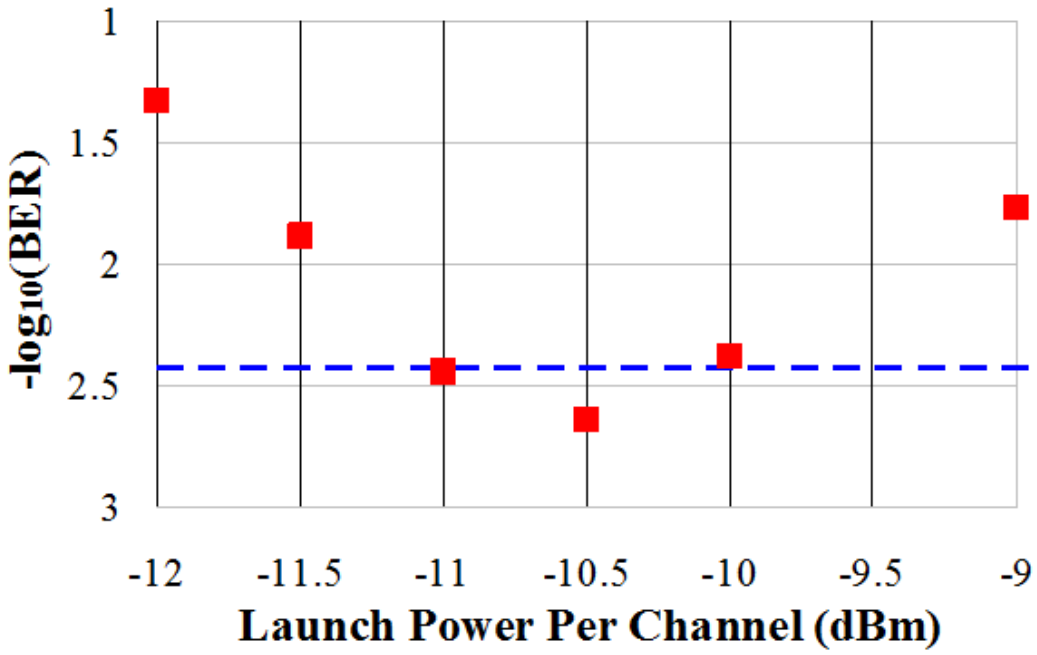

Fig. 3.14. BER vs. per channel launch power, for the center channel (1547.715 nm), measured after 7,321.5 km of transmission, where the FEC threshold is shown as a blue dashed line.

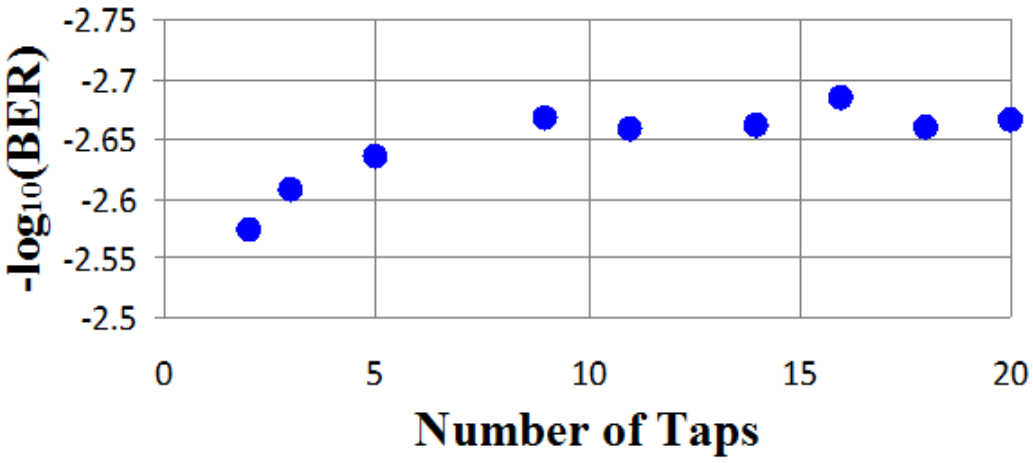

Fig. 3.15. Approximate adaptive equalization tap optimization at -10.5 dBm launch power.

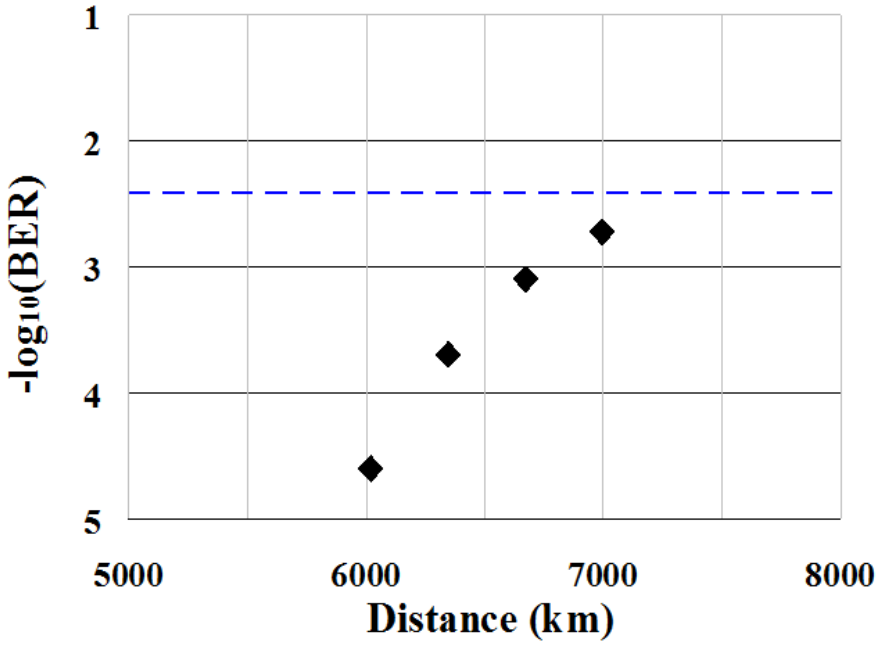

Fig. 3.16. BER vs. distance for the center channel (1547.715 nm), for launch power ≈ -10.5 dBm.

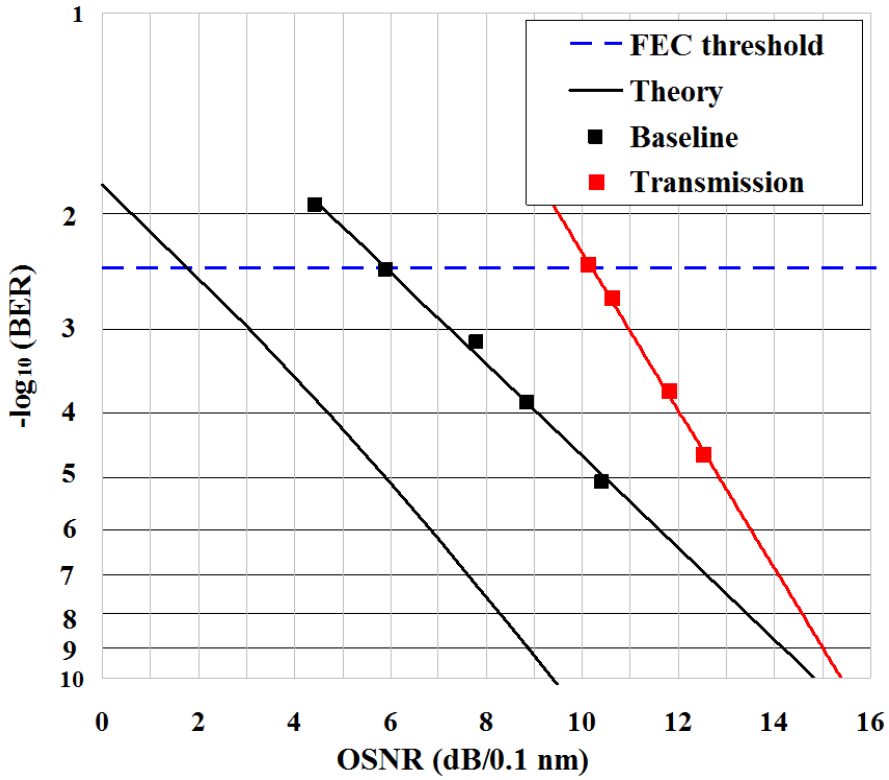

Fig. 3.17. Receiver sensitivity measurements for NRZ-BPSK after transmission in the recirculating loop (red squares), compared against the baseline (black squares). The "Theory" represents Eq. (1).

The coherent receiver recorded BER measurements with adaptive equalization enabled. A distance of approximately 7,000 km was attained for the center channel, when the channel launch power was -10.5 dBm. At longer distances, the FEC threshold was exceeded. These measurements of BER for varying distances are summarized in Fig. 3.16. Having measured the OSNR for each BER point in Fig. 3.16, the data was compared against the baseline (back-to-back) receiver sensitivity (Fig. 3.17). The OSNR penalty between the back-to-back and transmission curves at the FEC threshold was approximately 4 dB/0.1 nm. These two curves diverge as OSNR decreases (distance increases), and transmission impairments become increasingly dominant.

3.3.3 Polarization attraction after recirculating loop transmission

In this section, polarization attraction (PA) was employed on the central NRZ-BPSK channel, after transmission in the recirculating loop (RL), i.e. the signal was now directed to the PA module. Without PA transmission distances ≈ 7,000 km are achievable before reaching the selected FEC threshold, see Fig. 3.16 and Fig. 3.17 with an OSNR of ≈ 10 dB / 0.1 nm. However, the penalty associated with the G-M effect in section 3.3.1 precluded PA at distances greater than ~2,500 km due to the accumulation of ASE. Dispersion compensation may be carried out algorithmically in the coherent receiver, obviating the need for periodic dispersion compensation. Without periodic dispersion compensation and over long-haul distances greater than 1,000 km, dispersion severely broadens the signal, lowering its peak power, and making it difficult to achieve the requisite peak power for PA in the HNLF. Consequently, transmission was carried out with periodic dispersion compensation.

To test the efficacy of PA to transmission impairments, all components up to the LNF-EDFA, are replaced by the RL shown in Fig. 3.12. Moreover, the Transmitter was replaced by the DWDM transmitter of Fig. 3.11. Fig. 3.18 shows the Poincaré sphere traces, when PA was employed. Qualitatively, the two traces are similar. Note that a different polarization analyzer from the one used in [48] was used for this report

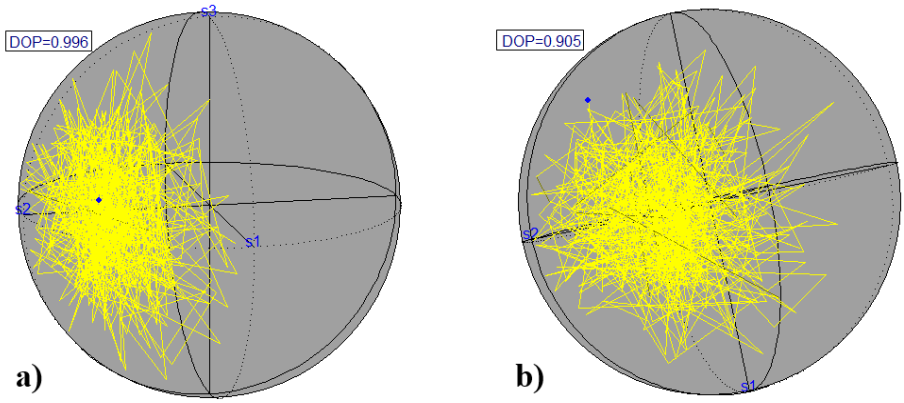

Fig. 3.18. Poincaré spheres for (a) ASE-loaded polarization attraction, and (b) long-haul transmission followed by polarization attraction. The traces were captured for the center NRZ-BPSK channel (1547.715 nm) using a trigger-capable polarization analyzer.

due to triggering capabilities. The captured Poincaré spheres in Fig. 3.19 demonstrate the efficacy of PA post-transmission in the RL. As the transmission distance is increased, the PA is seen to lose its efficiency, and to deviate, in terms of the output DOP, from the trend established at the shorter distances due to a degraded receiver OSNR. However, the PA output DOP remained above 90% for transmission distances up to 2,440.5 km, which includes those used in the receiver sensitivity measurement (Fig. 3.20). With the PA module employed in the receiver chain, eight circulations (1,301.6 km) were necessary to observe BER on the coherent receiver, otherwise the signal was received error-free. The received spectrum prior to demultiplexing and PA is in Fig. 3.20. Fig. 3.21 shows the receiver sensitivity measurements for post-transmission PA (red circles). The post-transmission PA measurements were taken after 8–15 circulations (1,301.6–2,440.5 km respectively), and all for a PA output DOP > 90%, as seen in Fig. 3.19. AE was enabled over the entire data set. Each measurement point of the post-transmission PA is found to be within 1.5 dB of the ASE-loaded back-to-back PA case, demonstrating that PA

impairments dominated those due to RL transmission. At the FEC threshold, the BER performance for ASE-loaded and RL cases were within 1.5 dB.

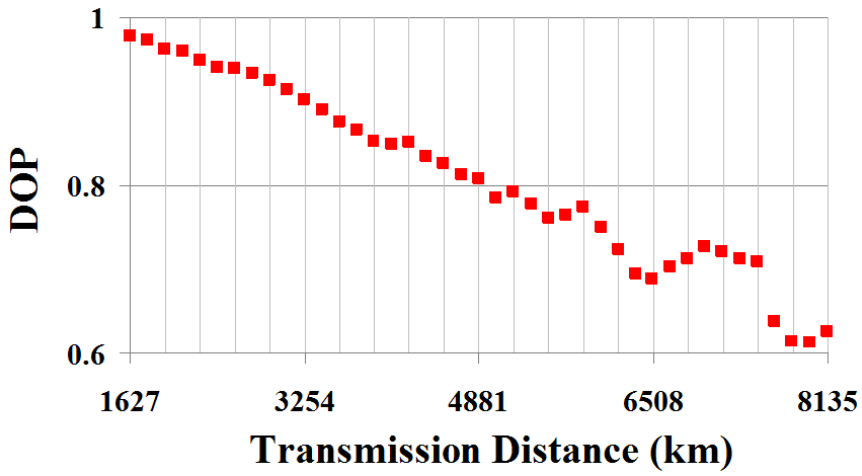

Fig. 3.19. DOP as a function of recirculating loop transmission distance when the DOP was measured after the polarization attraction module. One circulation is equivalent to 162.7 km. The data was captured using a triggered polarization analyzer.

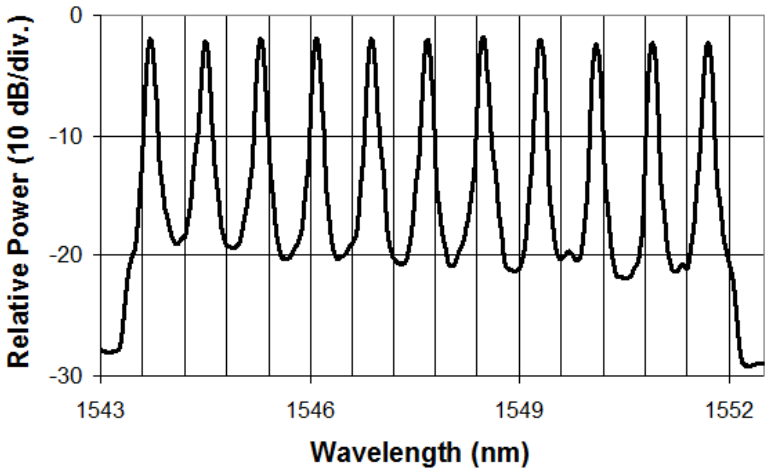

Fig. 3.20. Received spectrum at a resolution bandwidth of 0.1 nm, prior to polarization attraction in the HNLF. The transmission distance in the recirculating loop was 2,340.8 km (14 circulations).

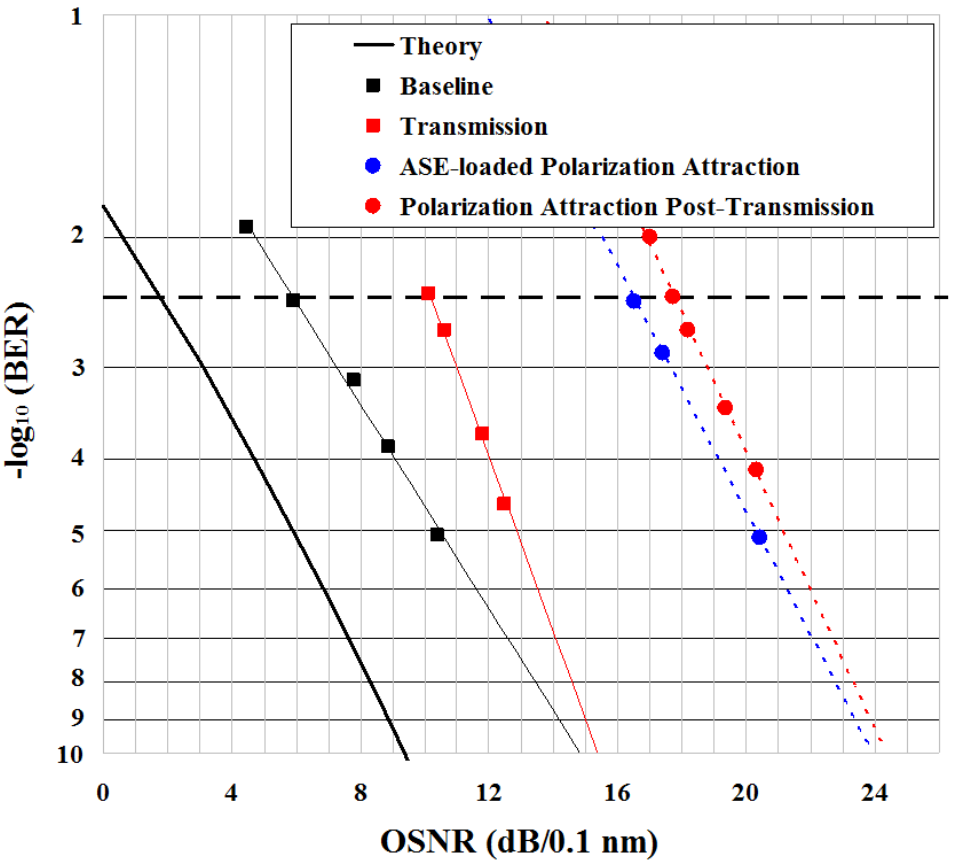

Fig. 3.21. Receiver sensitivity measurements for pol. attracted NRZ-BPSK after transmission in the recirculating loop (red circles), compared against the ASE-loaded PA (blue circles), the transmission (red squares), and the back-to-back (or baseline) configuration (black squares). The PA measurements post-transmission were taken after 8-15 circulations (1,301.6 – 2,440.5 km). The "Theory" represents Eq. (1).

Fig. 3.22 shows constellations captured at the FEC threshold for each experimental case in Fig. 3.21. Comparing constellations of baseline transmission and ASE-loaded PA in Figs. 3.22(b) and 3.22(c), respectively, the transmission degradations in baseline transmission appear to be

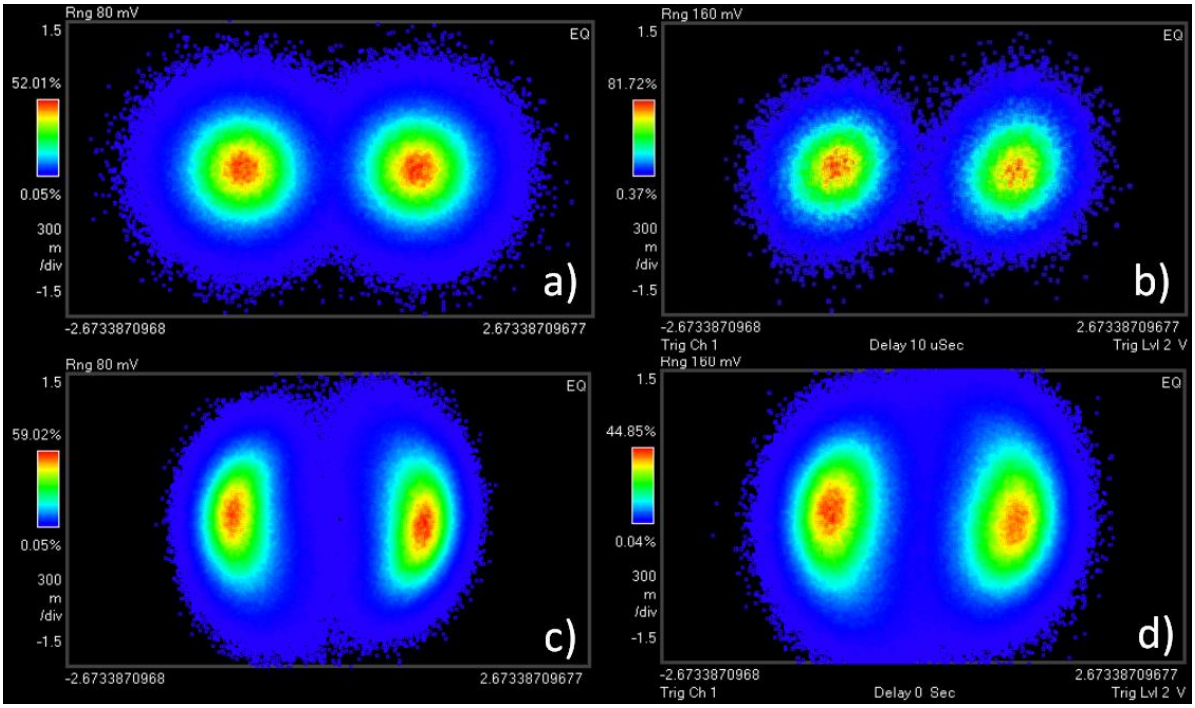

Fig. 3.22. Constellations at the FEC threshold for (a) baseline, (b) transmission, (c) ASE-loaded polarization attraction, and (d) polarization attraction post-transmission. The OSNR from (a) to (d) was ≈ 5.9 dB/0.1nm, 10 dB/0.1nm, 16.5 dB/0.1nm, and 17.7 dB/0.1nm.

much less significant than those of ASE-loaded PA. The constellation in Fig. 3.22(d) suffers from impairments due to long-haul transmission and PA, but still appears most similar to Fig. 3.22(c), since the nonlinear impairments in the HNLF dominate.

3.4 Summary and conclusions

For the first time to the authors' knowledge, polarization attraction of a scrambled 10.7-GBaud NRZ-BPSK signal in an HNLF has been evaluated for robustness to transmission impairments. In a back-to-back transmission evaluation, polarization attraction was employed for a signal corrupted by ASE only. A receiver sensitivity penalty at the G.709.1 FEC threshold of ~10.5 dB relative to the baseline performance suggested that the addition of ASE significantly enhanced nonlinear impairments in the HNLF. For the long-haul transmission evaluation, polarization attraction resulted in a nearly identical BER relative to polarization attraction on an ASE-loaded signal. For both cases, receiver sensitivity measurements and qualitative constellation diagrams confirmed that the effect within the HNLF was an overwhelmingly dominant impairment to the efficacy of polarization attraction.

Before polarization attraction may be considered a feasible application in a practical fiber communication system link, the penalty due to the G-M effect in the nonlinear medium must be mitigated in future work. The source of the G-M effect, ASE, is intrinsically statistical; hence, full compensation for the G-M effect is not possible [65]. One potential approach to partially compensate for the G-M effect may be an all-optical phase sensitive amplifier (PSA) employed directly after polarization attraction [2]. A PSA may be implemented with one or two CW pumps co-propagating with the signal [66]. This method requires that the CW pump(s) add coherently to the signal, so additional carrier recovery/pump phase-locking [67] is necessary for a scenario when the original light source for the signal is unavailable. A more practicable solution is to

implement a PSA with a nonlinear optical loop mirror (NOLM) before polarization attraction. A modified NOLM setup [68] would mitigate amplitude fluctuations while adding no additional phase jitter, which would reduce the G-M effect in the HNLF during polarization attraction. Another more recent experimental demonstration of phase-sensitive regeneration was performed without a phase-locked loop using Brillouin amplification [69].

Chapter 4

Conclusions

4.1 Summary

The research presented in this dissertation investigated polarization attraction as an all-optical polarization regeneration technique, which may serve as an alternative solution to reducing PDL across polarization-sensitive devices or NOSP's. The experimental configuration was chosen to test the efficacy of polarization attraction for a 10.7-GBaud BPSK signal after experiencing the combination of polarization scrambling, amplified spontaneous emission noise, and nonlinear impairments encountered during long-haul fiber transmission. Polarization attraction proof of principle demonstrations were performed in a low-dispersion HNLF with a nonlinear coefficient of $11W^{-1}km^{-1}$. A counter-propagating CW pump was required to maximize nonlinear cross-polarization interactions, effectively localizing the signal's randomly-varying SOP towards a stable SOP after the HNLF.

To the extent of the author's knowledge, PA has only been attempted for OOK, pulse-train, and CW signals. The work presented in this dissertation is the first demonstration of PA may be applied to a BPSK signal in a back-to-back configuration. The purpose of completing this initial step was to demonstrate the technique's potential applications to PSK signals commonly used in long-haul fiber transmission. In this first experiment, a 10.7-GBaud NRZ-BPSK signal was launched into the HNLF at 0.32 W along with a counter-propagating CW pump launched at 1.4 W. Through Kerr cross-

polarization interactions inherent to the fiber, the SOP of the signal was localized to a tight spot on the Poincaré sphere, and the DOP of the signal was maximized > 90%. To test the efficacy of the attracted DOP, the signal was passed through an undriven modulator to introduce PDL and emulate a polarization-sensitive device or NOSP operation. Without PA, the undriven modulator created amplitude fluctuations that lead to a severely distorted eye-diagram and loss of BER synchronization. With attraction engaged, amplitude fluctuations were mitigated and the receiver sensitivity penalty relative to baseline performance was < 0.5 dB for a BER of 10^{-9} and negligible for a BER at the G.709.1 FEC threshold. The results of the first experiment showed that PA may be applied to BPSK signals in the counter-propagating configuration previously only demonstrated for OOK, pulse-train, and CW signals.

The next two experiments presented in this work evaluated the robustness of PA to transmission impairments. At first, only ASE was increasingly added to the signal before experiencing PA, which revealed the next new challenge for future work: overcoming the Gordon-Mollenauer (G-M) effect. The ASE noise was artificially injected onto the signal via attenuation followed by re-amplification with a LNF-EDFA, while keeping the signal launch power into the HNLF constant. The lower OSNR of the signal revealed the G-M effect in the HNLF as the source of a significant impairment to the signal's receiver sensitivity. According to the G-M effect, the interaction of ASE with nonlinearity caused ASE-induced amplitude fluctuations to convert to phase fluctuations via SPM and/or XPM of the signal during propagation in the HNLF. A quantitative analysis of the G-M effect within the HNLF was provided as a comparison against

experimental measurements. This analysis explains that while the ASE-loaded PA measurements show a penalty of 10.5 dB relative to the baseline measurements, this penalty is actually predicted by the G-M effect's phase noise translated to a BER penalty.

In a third and most complex experiment, the robustness of polarization attraction was evaluated when applied to a BPSK signal after it endured long-haul transmission in a 24-channel multi-format DWDM system emulated by a 162-km recirculating loop. The goal of this final experiment was to test polarization attraction on a signal that was not only was loaded with ASE noise, but also accumulated long-haul transmission impairments, arising due to the interaction of dispersion, nonlinearity, PMD, and ASE. The experimental results showed a small additional receiver sensitivity penalty, relative to the ASE-loaded case. These results demonstrated that when the signal accumulates ASE, either during long-haul transmission or artificially in the transmitter, the resulting G-M effect within the attraction medium can diminish the efficacy of polarization attraction. Before polarization attraction may be considered a feasible application in a practical fiber communication system link, the penalty due to the G-M effect in the nonlinear medium must be mitigated in future work. Section 4.2 provides some potential avenues of future exploration in solving this challenge.

4.2 Future work

4.2.1. Phase sensitive amplification

On potential solution to partially compensating for the phase noise produced by the G-M effect could be utilizing a phase sensitive amplifier (PSA) after polarization attraction. In one implementation of a PSA, a CW pump and the signal co-propagate through a hybrid optical phase squeezer (HOPS) [70]. This method requires phase-locking between the pump and signal, maintained by a phase-locked loop (PLL), to stabilize long-term operation. As a consequence, this configuration unrealistically assumes that the original light source for the signal is available. Another implementation of a PSA can be demonstrated with a NOLM [71], which does not require a phase-locking stabilization. One final implementation of a PSA worth mentioning is the experimental demonstration performed in [69] via Brillouin amplification, which requires a CW pump but without the need for a phase-locked loop.

Each of these suggested implementations for the PSA are sensitive to polarization fluctuations. This may not be a significant issue if polarization attraction is employed before the PSA so that the DOP > 90%. In an experiment to evaluate a PSA's potential sensitivity to polarization, PA was employed as demonstrated in Chapter 2 followed by a second nonlinear medium (photonic crystal fiber) where FWM was performed. FWM is known to be sensitive to polarization and served as emulation for a polarization-sensitive PSA implementation. Receiver sensitivity results after FWM showed an OSNR penalty < 0.5 dB for a BER~10^{-9} most likely due to the DOP being attracted to 90% instead of an ideal 100%, before FWM. This experiment demonstrates that if a PSA were used after

attraction to mitigate phase noise, then a penalty of at least 0.5 dB may be added to the receiver sensitivity performance. This may be a reasonable trade off if the phase-noise receiver sensitivity penalty is reduced by even a few dB, considering that the penalty of ASE-loaded PA relative to baseline is more than 10 dB of OSNR.

Chapter 5

Appendix: Estimation of the penalty due to the Gordon-Mollenauer effect

5.1 Introduction

According to [50], error-free long-haul transmission is achievable for a NRZ-BPSK signal, so long as the mean nonlinear phase shift (NLPS) $\langle \varphi_{NL} \rangle \approx 1$ rad, which ensures the minimum phase variance for the received signal. The analysis was based on the assumption of two degrees-of-freedom (DOF), and matched-filter reception. The goal of this section is to apply the theory to the HNLF, in order to explain the large penalty experienced by the signal during polarization attraction. Although a significant penalty would be expected due to the magnitude of the acquired NLPS in the HNLF, a penalty as large as ≈ 10 dB relative to the baseline NRZ-BPSK would require some additional verification. The following analysis is based on that of [61,62], which is a much more rigorous derivation of the G-M effect.

In general, a signal of bandwidth *B* and symbol duration *T* will have $2K = 2BT$ DOFs, according to the sampling theorem [50]. A DOF is represented by one of a complete orthonormal set of *real* functions that span the signal field. A set of sinc-functions can be used as such to reconstruct the signal in the time domain. For the nomenclature used, the highest frequency component in the signal's spectrum is at $B/2$ Hz, so the signal can be completely described by a set of samples spaced at $1/B$ s, in the time domain.

Alternatively, a signal's field can be described by a total of K complex orthonormal basis functions F_k,

$$s(t) = \sum_{k=0}^{K-1} s_k F_k(t) \tag{5}$$

subject to

$$s_k = \int_{-\infty}^{\infty} s(t) F_k^*(t) dt \tag{6}$$

$$\int_{-\infty}^{\infty} F_m(t) F_n^*(t) dt = \delta_{mn} \tag{7}$$

Similarly, the ASE field (considered AWGN in the derivation) may also be described by K complex orthonormal basis functions,

$$n(t) = \sum_{k=0}^{K-1} N_k F_k(t), \tag{8}$$

with expansion coefficients given by

$$N_k = \int_{-\infty}^{\infty} n(t) F_k^*(t) dt \tag{9}$$

The real and imaginary parts of such coefficients are considered to be identically distributed, independent (i.i.d.) Gaussian random variables. Then the first and second order statistics of these ASE coefficients are given by

$$\langle N_k \rangle = 0 \tag{10}$$

$$\langle N_k N_k \rangle = 0 \tag{11}$$

$$\langle N_m N_n^* \rangle = \rho \delta_{mn} = n_{sp} h\nu (G-1) \delta_{mn} \tag{12}$$

where the expectation of the product of real and imaginary parts of a coefficient vanishes due to orthogonality. The modulus-squared of a coefficient, which represents energy, is a χ^2-distributed random variable of two DOFs. When the inner product Eq.(12) exists, it is construed as the ASE power spectral density (PSD) per unit-bandwidth, per polarization state. It has units of $h\nu$ per unit-bandwidth or [m^2kg/s^2] = J, conventionally stated as W/Hz. At this juncture, no assumptions are made about the basis functions - other than that a basis function has units of $s^{-1/2}$ to ensure a dimensionless result for the inner product of any two such functions.

5.2 NRZ-BPSK transmitter

The NRZ-BPSK signal is generated using a single-drive MZM optically driven by a laser at a frequency ν_0. It is biased at V_π (its transmission null), and driven at $2V_\pi$ by the AC-coupled electrical baseband NRZ-OOK symbol a_n, parenthesized in the numerator of the exponent:

$$s(t) = P^{1/2} \exp\left(i\pi \frac{V_\pi + 2V_\pi \cdot \left(a_n \mathrm{rect}\left(\frac{t_n}{T}\right) - \frac{1}{2} \right)}{2V_\pi} \right) \tag{13}$$

which is the slowly varying envelope (SVE) of the signal's optical field produced by the MZM. The symbol duration is represented by T. The rapidly changing carrier $\exp\left(-2i\pi\nu_0 t\right)$ is the term which multiplies the SVE to yield the time dependence of the optical field. The above expression may be alternatively expressed in terms of a cosine of a real argument. The amplitude in Eq.(13) accounts for the laser power and MZM propagation losses. The expression may be simplified to

$$s(t) = P^{1/2} \exp\left(i\pi a_n\right) \mathrm{rect}\left(\tfrac{t_n}{T}\right) \tag{14}$$

The n-th instant t_n is a contraction for (t - nT), and where a_n may be considered to be symbolically either a solitary ONE or ZERO with identical probabilities and represented temporally by the rect-function. This is a good approximation in practice since the baseband pulses are super-Gaussian in nature, with rise-/fall-times ≈ T/10 at 10.7-GBaud, assuming proper component selection. A solitary bit should be adequate without loss of generality, since the MZM output power is constant for BPSK except during relatively brief bit-transitions, irrespective of whether the baseband data is a ZERO or a ONE. Then the peak power is independent of the baseband pattern encoding the optical carrier. This expression neglects impulse response effects such as pattern-dependence in the transmitter, which would lead to a pattern-dependent output power, and to a possible penalty upon reception. The expression can be easily redefined in terms of an orthonormal basis function F_0satisfying the orthonormality condition in Eq.(7)

$$s(t) = E^{1/2} s_n \frac{\mathrm{rect}\left(\tfrac{t_n}{T}\right)}{T^{1/2}} = E^{1/2} s_n F_0(t) \tag{15}$$

where s_n represents the exp-term in Eq.(14). The rect-function can serve as a basis function for the electrical baseband signal, since any cluster of consecutive ONES or ZEROS could be expressed in terms of an expansion of rect-functions. $F_0(t)$ also represents the zeroth-order approximation of the main lobe of the sinc function, which is a basis function used for reconstruction in Shannon's original sampling theorem. To obviate the need for joint probability density function (p.d.f.)'s in the following analysis, the signal is considered deterministic.

In the experiment, three amplifiers are used in tandem to launch the signal into the HNLF. For its proper operation, the HPA required a pre-amplifier, which was comprised of two amplification stages with a 0.45-nm interstage filter. The output of the pre-amplifier was once again filtered, by 1-nm filter, to suppress low-power, out-of-band ASE. Based on Frii's amplifier theory, the signal's noise figure would be expected to be dominated by the pre-amplifier. For this analysis, it will be assumed that the entire amplifier chain, along with its attendant filters, is considered as one amplifier, which imparts gain *G* to the MZM output, and adds ASE within a 0.45-nm bandwidth to the amplified signal, resulting in the amplified signal input to the HNLF,

$$s_{in}(t) = G^{1/2} s(t) + n(t) \tag{16}$$

For a complete representation of ASE, an infinite number of basis functions would be required. However, only the ASE components lying in the signal space are relevant to its matched-filter reception. The remaining components would be orthogonal to the signal. This argument would also be approximately valid as long as the signal bandwidth is not significantly exceeded by the filter's bandwidth, which was also argued in [31]. Consequently, a maximum of 2 DOFs are also used for the ASE field, yielding

$$n(t) = \left(N_{0r} + iN_{0i} \right) F_0(t) \tag{17}$$

Finally, the SVE of the *amplified* signal is given by

$$s_{in}(t) = G^{1/2} E^{1/2} s_n F_0(t) + n(t) = E_0^{1/2} s_n(t) + n(t) \tag{18}$$

The peak energy incorporates the gain factor, and the temporal quantities incorporate the sole basis function $F(t)$. Substituting Eq.(17) into Eq.(18), it is observed that the in-phase

ASE component results in amplitude fluctuations, whereas the quadrature ASE component yields a phase shift. Both components however, will contribute to the mean NLPS, and more significantly at relatively low OSNRs. The equation is also expressible in polar form as

$$s_{in}(t) = \left(\left| E_0^{1/2} s_n + N_{0r} \right|^2 + \left| N_{0i} \right|^2 \right)^{1/2} \left| F_0(t) \right| \exp\left(i \tan^{-1}\left(\frac{N_{0i}}{E_0^{1/2} s_n + N_{0r}} \right) \right) \tag{19}$$

5.3 Propagation in the HNLF

Since the HNLF is a standard fiber (although with a highly reduced effective area) with principle states of polarization (PSPs), propagation of the optical field is not governed by the scalar nonlinear Schrodinger equation (NLSE), but by the Manakov equation for the signal's Jones vector **A**,

$$\left(\frac{\partial}{\partial z} + \frac{\alpha}{2} + \frac{\Delta\beta_1}{2} \mathbf{J} \frac{\partial}{\partial t} + i \frac{\beta_2}{2!} \frac{\partial^2}{\partial t^2} - \frac{\beta_2}{3!} \frac{\partial^3}{\partial t^3} \right) \mathbf{A} = \frac{8}{9} i\gamma \left| \mathbf{A} \right|^2 \mathbf{A} \tag{20}$$

where the electric field of the optical signal is described by the vector

$$\mathbf{E}(\mathbf{r}, t) = \left(\mathbf{x}\, A_x(z,t) U(x,y) + \mathbf{y}\, A_y(z,t) V(x,y) \right) \exp\left(i\bar{\beta}(\nu_0) z - 2i\pi\nu_0 t \right) \tag{21}$$

The vector fields *U* and *V* describe the transverse spatial dependence of the electric field **E** of the optical field. The two vectors possess different eigenvalues resulting in different group velocities and necessitating the use of a mean propagation constant. The SVE complex coefficients $A_x(z, t)$ and $A_y(z, t)$ constitute the Jones vector of the optical field, which describes the SOP of the field at (z, t). The Jones vector incorporates $s_{in}(t)$. The vector components are properly normalized to reproduce the average power of $s_{in}(t)$.

Using the above expression for the electric field in the derivation, averaging over the transverse spatial dependence, as well as over the complex exponential, results in the Manakov equation after a few manipulations. The second term on the LHS expresses propagation loss, the third term, PMD, and the last two terms pertain to dispersion. **J** is the birefringence matrix, and is a random unitary 2 x 2 matrix, a function of (*z*, *t*), and results, along with the deterministic birefringence $\Delta\beta_1$, in random group velocities for the two polarization components. In the frequency domain, its Jones eigenvectors represent the fiber's PSPs. Due to a low PMD coefficient of 0.05 ps/km$^{1/2}$, and at 10.7-GBaud, the HNLF PMD may be considered negligible. The 1/9-th reduction in the nonlinear coefficient arises due to averaging the SPM-term over the fiber's birefringence fluctuations. The resultant 8/9th-coefficient has to be retained in the equation, even when PMD is deemed negligible [72,73]. Due to the HNLF's large dispersion and dispersion-slope lengths at 10.7-GBaud, terms representing dispersion may also be ignored, leading to the closed-form solution at the output plane of the HNLF

$$\mathbf{A}(L,t) = \mathbf{A}(0,t)e^{-\alpha L/2}\exp\left(i\tfrac{8}{9}\gamma\left|\mathbf{A}(0,t)\right|^2\int_0^L e^{-\alpha z}dz\right) = \mathbf{A}(0,t)e^{-\alpha L/2}\exp\left(i\tfrac{8}{9}\gamma\left|\mathbf{A}(0,t)\right|^2 L\right) \quad (22)$$

The effective length is practically identical to the physical length *L* due to the low propagation loss of the HNLF. At the input plane (*z*=0) of the HNLF, and for a polarization-stable field, the field is assumed to have the relatively *static* Jones vector

$$\mathbf{A}(0,t) = s_{in}(t)\left(\mathbf{x}\,A_x(0,t) + \mathbf{y}\,A_y(0,t)\right) \quad (23)$$

The field's launch angle relative to the HNLF PSPs is defined by the magnitudes of the vector's components, and the launch angle is quite stable in practice. However, the

components' relative phase can still randomly drift with time; but a polarization analyzer observation revealed that the SOP drift rate was slow on the order of seconds, and thus much slower than the Baud-rate. The relative phase may therefore be considered constant. It was also found that with the undriven MZM bypassed, the receiver sensitivity measurement on the signal output by the HNLF was independent of polarization scrambling up to ≈ 12 kHz, implying negligible HNLF PDL.

5.4 The Gordon-Mollenauer theory for HNLF

In the output signal expression extracted from the solution of the Manakov equation for the optical field, the SPM-induced NLPS may be expanded into a series

$$s_{out}(t) = T^{1/2} e^{-\alpha L/2} \left(E_0^{1/2} s_n + N_0 \right) F_0(t) \sum_{k=0}^{\infty} \frac{1}{k!} \left(\frac{i \frac{8}{9} \gamma L}{T} \right)^k \left| E_0^{1/2} s_n + N_0 \right|^{2k} \tag{24}$$

At the receiver, the demodulator eliminates the parts of the signal irrelevant to the detection process. Correlation demodulation entails taking an inner product of the received signal with a span function $F^*(t)$ over the duration of the symbol,

$$r_s = \int_{-\infty}^{\infty} s_{out}(t) F_0^*(t) dt = T^{1/2} e^{-\alpha L/2} \left(E_0^{1/2} s_n + N_0 \right) \exp\left(\frac{i \frac{8}{9} \gamma L}{T} \left| E_0^{1/2} s_n + N_0 \right|^2 \right) \tag{25}$$

Equivalently, the integration may be recast as a convolution with a filter of the impulse response $h(t) = F^*(T-t)$. When the filter's impulse response assumes the form $h(t) = s_{out}(T-t)^*$, the filter is termed "matched". The signal-to-noise ratio (SNR) is generally defined as

$$\text{SNR} = \frac{|r_s(T)|^2}{\left\langle |r_N(T)|^2 \right\rangle} = \frac{\left| \int_{-\infty}^{\infty} s_{out}(\tau) h^*(t-\tau) d\tau \right|^2}{\rho \left| \int_{-\infty}^{\infty} h^*(t-\tau) d\tau \right|^2} = \frac{E_0}{\rho} \tag{26}$$

where the final result is only attained for matched filter reception. The SNR is then the ratio of the energy-per-bit (E) to the unilateral ASE power spectral density per polarization, ρ. SNR is identical with the Q-factor defined in [50]. This is a standard metric used for all non-optical communications systems and is Baud-rate independent [74]. SNR can be converted to OSNR, a quantity both Baud-rate and bandwidth dependent,

$$\mathrm{OSNR} = \frac{R}{2B_o}\mathrm{SNR} = \frac{R}{2B_o}Q \tag{27}$$

The matched-filter receiver provides no advantages for the RZ-format relative to the NRZ-format (as might be the case in practice); but the RZ duty cycle can significantly enhance the NLPS, and therefore, the nonlinear phase noise (NLPN). The phase of the demodulated signal is just the sum of the phases due to each term involved in the product in Eq.(25):

$$\varphi = \tan^{-1}\left(\frac{N_{0i}}{E_0^{1/2}s_n + N_{0r}}\right) + \frac{8\gamma L}{9T}\left(\left(E_0^{1/2}s_n + N_{0r}\right)^2 + N_{0i}^2\right) \tag{28}$$

which was found with the help of Eq.(17). The first term expresses the linear phase noise due to amplification, while the second term, the NLPN, due to the interaction of ASE with SPM. The two random processes are in a sum that also involves the BPSK signal itself. In the G-M theory, these processes are considered to be statistically independent, as much as the signal and the ASE. In reality, this is not the case, as will be explained in Section 5.5. Moreover, neither of the two terms is Gaussian distributed, in general. However, these assumptions expedite the analysis, resulting in compact, approximate solutions. The first term of Eq.(28) is now considered. The argument is the ratio of two

i.i.d. Gaussian random variables, resulting in a Cauchy-distributed random variable. The Cauchy p.d.f. is not defined in terms of the mean and the variance, which makes further progress difficult. However, under the assumption of a high received SNR that would render the in-phase ASE component negligible relative to the signal amplitude, a Taylor series expansion can be then be carried out and truncated to its first-order,

$$\tan^{-1}\left(\frac{N_{0i}}{E_0^{1/2}s_n + N_{0r}}\right) \approx \frac{N_{0i}}{E_0^{1/2}s_n} \tag{29}$$

which renders the first term in Eq.(28) Gaussian-distributed random variable. The assumption of high SNR for the above approximation may be violated for signals encoded with FEC, which require significantly lower SNR to achieve a target BER. The phase can be re-arranged as

$$\Phi \approx \frac{8\gamma L\, E_0}{9T} + \frac{N_{0i}}{E_0^{1/2}s_n} + \frac{8\gamma L}{9T}\left(2N_{0r}E_0^{1/2}s_n + \left|N_0\right|^2\right) \tag{30}$$

The statistical average is now computed, using the statistics of the ASE Eq.(10)-Eq.(12), and recalling that signal and noise are assumed to be statistically independent,

$$\langle\Phi\rangle \approx \frac{8\gamma L\, E_0}{9T} + \frac{8\gamma L\, \rho}{9T} = \frac{8\gamma L E_0}{9T}\left(1+\frac{\rho}{E_0}\right) = \langle\Phi_{\mathrm{NL}}\rangle\left(1+\frac{1}{Q}\right) \tag{31}$$

where $\Phi_{\mathrm{NL}} = 8/9\gamma P_0 L$ is the NLPS and can be used to simplify Eq.(30). The second parenthesized term may not be negligible at the selected FEC threshold, when SNR can be << 10. To evaluate the variance of the phase Eq.(30), the expected value of the quantity $(\varphi - \langle\varphi\rangle)^2$ is computed, with the result

$$\left\langle \delta\Phi^2 \right\rangle \approx \frac{\left\langle N_{0i}^2 \right\rangle}{E_0} + 2\frac{\left\langle N_{0r}^2 \right\rangle}{E_0}\left\langle \Phi_{NL} \right\rangle^2 - \left(\frac{\left\langle |N_0|^2 \right\rangle}{E_0}\left\langle \Phi_{\mathrm{NL}} \right\rangle \right)^2 \tag{32}$$

after which ASE coefficients of orders higher than 2 were neglected. Eq.(32) demonstrates that the phase variance depends on both the linear and nonlinear phase noises. The first term shows that the PSD due to the ASE quadrature component contributes to the linear phase noise and is mitigated solely through division by the signal's energy. The second term yields the NLPN, is due to the PSD of the in-phase component of the ASE, which is amplified though cross-modulation with the NLPS. The in-phase and quadrature components represent the 2 DOF's adopted for this derivation. The last term in Eq.(30) is a subtractive correction based on the cross-modulation of the total ASE PSD with the NLPS and is a consequence of carrying out the variance. It may not be negligible around the FEC threshold, where SNR can be relatively low. Upon substitution of $\Phi_{\mathrm{NL}} = 8/9\gamma P_0 L$ in Eq.(32) and using Eq.(12), the dependence on the signal energy is revealed to be

$$\left\langle \delta\Phi^2 \right\rangle \approx \frac{\rho}{2E_0} + 2\left(\frac{8\gamma L}{9T} \right)^2 \rho E_0 - \left(\frac{8\gamma L}{9T} \right)^2 \rho^2 \tag{33}$$

The first term which represents the *linear* phase noise, is inversely proportional to the signal's energy, whereas the second term, the *nonlinear* phase noise, is directly proportional to it. The existence of an extremum may be explored through differentiation with respect to the signal energy E_0, yielding a minimum mean NLPS of

$$\left\langle \Phi_{NL} \right\rangle = 0.5\,\mathrm{rad}. \tag{34}$$

after using $\Phi_{NL} = 8/9\gamma P_0 L$. The minimum variance is then, in terms of SNR Eq.(26) or Q, found by substitution of Eq.(34) into Eq.(32)

$$\left\langle \delta\Phi^2 \right\rangle_{\min} \approx \frac{1}{Q_{MF}} - \frac{1}{4Q_{MF}^2} \tag{35}$$

since for a given BER, the matched filter (MF) receiver requires the lowest Q, i.e. Q_{MF}, for a given BER. The minimum variance Eq.(35) represents an upper bound for the variance Eq.(33), which is restated as

$$\left\langle \varphi_{NL} \right\rangle^2 \left(2\frac{1}{Q} - \left(\frac{1}{Q} \right)^2 \right) + \frac{1}{2Q} \le \frac{1}{Q_{MF}} - \frac{1}{4Q_{MF}^2} \tag{36}$$

but for relatively high (O)SNRs, terms of order Q^{-2} may be ignored, resulting in the simplified condition, after a re-arrangement

$$Q \ge \tfrac{1}{2} Q_{MF} \left(1 + 4\left\langle \varphi_{NL} \right\rangle^2 \right) \tag{37}$$

where Q_{MF} is the quantity corresponding to the matched-filter BER

$$\text{BER} = \frac{1}{2}\text{erfc}\left(\sqrt{Q_{MF}} \right). \tag{38}$$

Alternatively, condition Eq.(37) may be re-expressed in terms of the OSNR Eq.(27), which is the measurable quantity. Then results the condition on the minimum *expected* experimental OSNR (referenced to a resolution bandwidth of B_o) required to achieve an experimentally observed BER, for an R-Baud BPSK signal experiencing a mean NLPS $\left\langle \Phi_{NL} \right\rangle$,

$$\text{OSNR} \ge \frac{R}{4B_o} \left(1 + 4\left\langle \Phi_{NL} \right\rangle^2 \right) \left(\text{erfc}^{-1}\left(2\text{BER} \right) \right)^2, \tag{39}$$

and assuming matched-filter reception, which is represented by the squared $erfc^{-1}$-term. Given a BER, a more accurate result may be obtained from a substitution of Eq.(38) into Eq.(36) and solving the resultant quadratic equation for *Q* (or OSNR). A commonly used BER metric in receiver sensitivity experiments is $BER_{EF} = 10^{-9}$, at which reception is considered error-free (EF). Due to the widespread usage of FEC technology, a relatively high BER may be corrected to $< 10^{-12}$. For ITU-T G.709.1 RS(255, 239) HD-FEC, the relevant BER to use in Eq. (39) is $BER_{FEC} = 3.8 \times 10^{-3}$.

5.5 An exact theory

An exact theory for the BER of a BPSK signal suffering the G-M effect has been reported for a long-haul transmission line, consisting of *N* dispersion-less, PMD-free amplified spans [75,76]. The 1-km HNLF used in the experiment can be considered to be negligible in terms of both dispersion and PMD, for 10.7-GBaud NRZ-BPSK, using a low linewidth laser. It may be assumed that the effective nonlinear phase shift due to propagation over the transmission line is identical to that generated by the HNLF, assuming that the relevant quantities are appropriately scaled.

The matched filter receiver BER for an NRZ-BPSK signal suffering nonlinear phase noise (NLPN) due to the G-M effect may be computed using the Fourier series expansion of a probability density function (p.d.f.). The p.d.f. is found from the joint characteristic function of the normalized NLPN and the phase of amplifier noise (ASE). For a given OSNR, the BER is exacerbated due to the dependence between the NLPN and the phase of ASE [76]. The probability of error or BER, was found to be related to the integral of the p.d.f. of the received phase Φ_r [77]

$$\mathrm{BER} = 1 - \int_{-\frac{\pi}{2}-\theta_c}^{\frac{\pi}{2}-\theta_c} p_{\Phi_r}(\theta)d\theta = \tfrac{1}{2} - \tfrac{2}{\pi}\sum_{n=0}^{\infty}\frac{(-1)^n}{2n+1}\Re\mathrm{e}\left[\Psi^*_{\Phi_r}(2n+1)e^{-i(2n+1)\theta_c}\right] \tag{44}$$

The p.d.f. is actually symmetric in the absence of the NLPN; but is broadened asymmetrically by the NLPN, depending on the magnitude of the NLPS. If the p.d.f. of the received phase were symmetric with respect to the mean NLPS $\langle\Phi_{\mathrm{NL}}\rangle = 8/9\gamma P_0 L$ (as in the previous section), the decision boundary would be centered at $\langle\Phi_{\mathrm{NL}}\rangle$, resulting in the decision angle of $\pm\frac{\pi}{2} - \langle\Phi_{\mathrm{NL}}\rangle$ for BPSK. In reality, the p.d.f. is not symmetrical in such a manner. Consequently, the decision boundary is expressed instead as $\pm\frac{\pi}{2} - \theta_c$. The characteristic function coefficient for Φ_r, are given by

$$\Psi^*_{\Phi_r}(2n+1) = \frac{\sqrt{\pi\lambda_n}}{2}\left[I_n\left(\frac{\lambda_n}{2}\right) + I_{n+1}\left(\frac{\lambda_n}{2}\right)\right]\Psi_{\Phi}\left(\left(2n+1\right)\frac{\langle\Phi_{\mathrm{NL}}\rangle}{\langle\Phi\rangle}\right)e^{-\lambda_n/2} \tag{45}$$

and is actually found from the joint characteristic function of the NLPN and the phase of ASE. The received phase is limited to be in [- π, π), and is generally expressed as the difference between the phase of the ASE and the normalized NLPN. Although the normalized NLPN and the phase of ASE are uncorrelated due to the expectation being $\langle\Phi_{\mathrm{NL}}\Theta\rangle = 0$, a dearth of correlation is not equivalent to independence for non-Gaussian random variables. The dependence is however, weak [49]. I_n is the modified Bessel function of the first kind, and *n*-th order, with argument

$$\lambda_n = \frac{Q}{\mathrm{sinc}\left[2\left(i\left(2n+1\right)\frac{\langle\Phi_{\mathrm{NL}}\rangle}{\langle\Phi\rangle}\right)^{1/2}\right]}, \tag{46}$$

where the sinc-function is defined as sin(x)/x, and $\langle\Phi\rangle$ is the mean *normalized* NLPN given by

$$\langle\Phi\rangle = Q + \tfrac{1}{2}\eta, \tag{47}$$

and

$$\eta = 2\frac{B_F}{B_o} \tag{48}$$

is the product of the number of polarizations, and the ratio of the -3-dB-bandwidth (0.45 nm or 56.25 GHz) of the receiver DWDM demultiplexer filter used in the experiment, to the resolution bandwidth (12.48 GHz). This factor is required to account for the cross-modulation of the out-of-band dual-polarized ASE, with the signal. Additionally, the marginal characteristic function of the *normalized* nonlinear phase noise is given by

$$\Psi_\Phi(\nu) = \sec(i\nu)^{\eta/2} \exp\left(Q\cdot(i\nu)^{1/2}\cdot\tan(i\nu)^{1/2}\right) \tag{49}$$

which was obtained from the non-separable joint characteristic function $\Psi_{\Phi,\Theta_n}(\nu,\omega)$ of the normalized NLPN and the phase of ASE, which is the two-dimensional Fourier transform of their joint p.d.f. $p_{\Phi,\Theta_n}(\varphi,\theta)$.

Lastly, the phase angle θ_c is critical to the resultant BER and deserves further discussion. Using the exact BER expression Eq. (44), the optimal θ_c was found to be smaller than the mean NLPS $\langle\Phi_{\mathrm{NL}}\rangle$,when the mean NLPS was smaller than ≈ 1.25 rad. At a low $\langle\Phi_{\mathrm{NL}}\rangle$, the p.d.f. of the received phase Φ_r spreads towards the positive phase so that the optimal $\theta_c < \langle\Phi_{\mathrm{NL}}\rangle$. At a high $\langle\Phi_{\mathrm{NL}}\rangle$, Φ_r is dominated by NLPN. Since the p.d.f. of

NLPN spreads towards the negative phase, the optimal $\theta_c > \langle \Phi_{NL} \rangle$. The latter was the case for the polarization attraction experiment, which required a NLPS of $\approx \pi$, necessitating a $\theta_c \approx 1.04 \langle \Phi_{NL} \rangle$ [76]. The difference between the low and the high $\langle \Phi_{NL} \rangle$ cases is ascribed to the interdependence of the NLPN and the phase of ASE.

5.6 Applicability of the two theories

Both the G-M theory and the exact theory assume matched-filter reception. It is well known that a matched filter is the optimal linear filter that maximizes the output signal SNR in the presence of additive white Gaussian noise. For non-Gaussian noise, this filter may not necessarily maximize SNR. Practical receivers can significantly deviate from matched filter reception, due to pattern-dependence, and ISI, among other impairments that are not generally Gaussian. At a minimum, both theories explored here are deficient in this respect, and bound to be in error when applied to experimental data. However, the assumption of a matched filter simplifies the analysis, since the optimal receiver for non-Gaussian noise is typically nonlinear and is dependent on the noise statistics that may not be available *a priori*. For non-Gaussian noise, a (projected) orthogonal matched filter may be more appropriate [77]. Further, the G-M theory assumes the received signal phase to be Gaussian in distribution, with no interdependence between the ASE phase and the nonlinear phase noise, both of which are approximations. By contrast, the exact theory demonstrates that neither process is Gaussian in distribution, nor are they independent of each other, and is thus more accurate.

Bibliography

1. Cisco Visual Networking Index. “The zettabyte era: trends and analysis,” Cisco White Paper (2017).
2. A. E. Willner, S. Khaleghi, M. R. Chitgarha, O. F. Yilmaz, “All-optical signal processing,” J. Lightw. Technol. **32**(4), 660–1030 (2014).
3. M. D. Feuer, and S. L. Woodward, “ROADMs: reconfigurable optics for agile networks,” Opt. and Photon. News, **26**(3), 36–43 (2015).
4. C. D. Poole and R. E. Wagner, “Phenomenological approach to polarization dispersion in long single-mode fibers,” Electron. Lett. **22**(19), 1029–1030 (1986).
5. J. Garnier, J. Fatome, and G. Le Meur, “Statistical analysis of pulse propagation driven by polarization-mode dispersion,” J. Opt. Soc. Amer. B **19**(9), 1968–1977 (2002).
6. M. Brodsky, N. J. Frigo, M. Boroditsky, and M. Tur, “Polarization mode dispersion of installed fibers,” J. Lightw. Technol. **24**(12), 4584–4599 (2006).
7. V. E. Chernov and B. A. Zon, “Depolarization of laser radiation in a nonlinear medium,” J. Opt. Soc. Amer. B **10**(2), 210–212 (1993).
8. A. Picozzi, “Entropy and degree of polarization for nonlinear optical waves,” Opt. Lett. **29**(14), 1653-1655 (2004).
9. H. Prakash and D. K. Singh, “Change in coherence properties and degree of polarization of light propagating in a lossless isotropic nonlinear Kerr medium,” J. Phys. B: At. Mol. Opt. Phys. **41**(4), 1-5 (2008).
10. K. Inoue, “Polarization Independent Wavelength Conversion Using Fiber Four-Wave Mixing with Two Orthogonal Pump Lights of Different Frequencies,” J. Lightw. Technol. **12**(11), 1916–1920 (1994).
11. B. C. Collings and L. Boivin, “Nonlinear polarization evolution induced by cross-phase modulation and its impact on transmission systems,” IEEE Photon. Technol. Lett. **12**(11), 1582–1584 (2000).
12. J. Hansryd, P. A. Andrekson, M. Westlund, J. Li, and P.-O. Hedekvist, “Fiber-Based Optical Parametric Amplifiers and Their Applications,” IEEE J. Sel. Topics Quantum Electron. **8**(3), 506-520 (2002).
13. H. Fukuda, K. Yamada, T. Tsuchizawa, T. Watanabe, H. Shinojima, and S. Itabashi, “Silicon photonic circuit with polarization diversity,” Opt. Exp. **16**(7), 4872-4880 (2008).
14. M. Barozzi, and A. Vannucci, “Dynamics of lossless polarization attraction,” Photon. Res. **3**(5), 229-233 (2015).
15. P. Morin, S. Pitois, and J. Fatome, “Simultaneous polarization attraction and Raman amplification of a lightbeam in optical fibers,” J. Opt. Soc. Amer. B **29**(8), 2046-2052 (2012).
16. J. Fatome, P. Morin, S. Pitois, and G. Millot, “Light-by- Light Polarization Control of 10-Gb/s RZ and NRZ Telecommunication Signals,” IEEE J. Sel. Topics Quantum Electron. **18**(2), 621-628 (2012).
17. M. Barozzi, and A. Vannucci, “Lossless polarization attraction of telecom signals: application to all-optical OSNR enhancement,” J. Opt. Soc. Amer. B **31**(11), 2712-2720 (2014).
18. M. Barozzi, A. Vannucci, and G. Picchi, “All-optical polarization control and noise cleaning based on a nonlinear lossless polarizer,” Proc. SPIE **9450**, 94501G (2015).
19. V. Costa Ribeiro, R. S. Luis, J. Manuel, D. Mendinueta, B. J. Puttnam, A. Shahpari, N. J. C. Muga, M. Lima, S. Shinada, N. Wada, and A. Teixeira, “All-Optical Packet Alignment Using Polarization Attraction Effect,” IEEE Photon. Technol. Lett. **27**(5), 541–544 (2015).
20. B. C. Collings and L. Boivin, “Nonlinear polarization evolution induced by cross-phase modulation and its impact on transmission systems,” IEEEPhoton. Technol. Lett. **12**(11), 1582–1584 (2000).
21. C. D. Poole and D. L. Favin, “Polarization-Mode Dispersion Measurements Based on Transmission Spectra Through a Polarizer,” J. Lightw. Technol. **12**(6), 917-929 (1994).
22. T. Yang, C. Shu, and C. Lin, “Depolarization technique for wavelength conversion using four-wave mixing in a dispersion-flattened photonic crystal fiber,” Opt. Exp. **13**(14), 5409-5415 (2005).
23. K. Mishina, S. Kitagawa, and A. Maruta, “All-optical modulation format conversion from on-off-keying based on nonlinearity in optical fiber,” Opt. Exp. **15**(13), 8444-8453 (2007).
24. J. E. Heebner, R. S. Bennink, and R. W. Boyd, “Conversion of unpolarized light to polarized light with greater than 50% efficiency by photorefractive two-beam coupling,” Opt. Lett. **25**(4), 257–259 (2000).
25. S. Pitois, and M. Haelterman, “Optical fiber polarization funnel,” in *Nonlinear Guided Waves and Their Applications*, 2001 OSA Technical Digest Series (Optical Society of America, 2001), paper MC79.

26. S. Pitois, J. Fatome, and G. Millot, “Polarization attraction using counter-propagating waves in optical fiber at telecommunication wavelengths,” Opt. Exp. **16**(9), 6646-6651 (2008).

27. J. Fatome, S. Pitois, P. Morin, and G. Millot, “Observation of light-by-light polarization control and stabilization in optical fibre for telecommunication applications,” Opt. Exp. **18**(15), 15311-15317 (2010).

28. P. Morin, J. Fatome, C. Finot, S. Pitois, R. Claveau, and G. Millot, “All-optical nonlinear processing of both polarization state and intensity profile for 40 Gbit/s regeneration applications,” Opt. Exp. **19**(18), 17158-17166 (2011).

29. V. V. Kozlov, J. Fatome, P. Morin, S. Pitois, G. Millot, and S. Wabnitz, “Nonlinear repolarization dynamics in optical fibers: transient polarization attraction,” J. Opt. Soc. Amer. B **28**(8), 1782–1791 (2011).

30. E. Assémat, S. Lagrange, A. Picozzi, H. R. Jauslin, and D. Sugny, “Complete nonlinear polarization control in an optical fiber system,” Opt. Lett. **35**(12), 2025-2027 (2010).

31. M. Guasoni, E. Assemat, P. Morin, A. Picozzi, J. Fatome, S. Pitois, H. R. Jauslin, G. Millot, and D. Sugny, “Line of polarization attraction in highly birefringent optical fibers,” J. Opt. Soc. Amer. B **31**(3), 572–580 (2014).

32. V. V. Kozlov and S. Wabnitz, “Theoretical study of polarization attraction in high-birefringence and spun fibers,” Opt. Lett. **35**(23), 3949-3951 (2010).

33. E. Assemat, D. Dargent, A. Picozzi, H. R. Jauslin, and D. Sugny, “Polarization control in spun and telecommunication optical fibers,” Opt. Lett. **36**(20), 4038-4040 (2011).

34. V. V. Kozlov, J. Nuño, and S. Wabnitz, “Theory of lossless polarization attraction in telecommunication fibers,” J. Opt. Soc. Amer. B **28**(1), 100-108 (2011).

35. V. V. Kozlov, J. Nuño, J. D. Ania-Castanon, and S. Wabnitz, “Theoretical Study of Optical Fiber Raman Polarizers With Counterpropagating Beams,” J. Lightw. Technol. **29**(3), 341–347 (2011).

36. P. J. Winzer, and R. Essiambre, “Advanced Modulation Formats for High-Capacity Optical Transport Networks,” J. Lightw. Technol. **24**(24), 4711-4728 (2006).

37. C. R. Menyuk, and B. S. Marks, “Interaction of Polarization Mode Dispersion and Nonlinearity in Optical Fiber Transmission Systems,” J. Lightw. Technol. **24**(7), 2806–2825 (2006).

38. D. David, D. D. Holm, and M. V. Tratnik, “Hamiltonian Chaos in Nonlinear Optical Polarization Dynamics,” Phys. Rep. **187**(6), 281-367 (1990).

39. A. Kobyakov, M. Sauer, and D. Chowdhury, “Stimulated Brillouin scattering in optical fibers,” *Adv. Opt. Photon.* **2(1)**, 1-59 (2010).

40. R. E. Newnham, and V. Sundar, “Electrostriction: Nonlinear Electromechanical Coupling in Solid Dielectrics,” J. Phys. Chem. B **101**(48), 10141-10150 (1997).

41. K. Inoue, T. Hasegawa, and H. Toba, “Influence of Stimulated Brillouin Scattering and Optimum Length in Fiber Four-Wave Mixing Wavelength Conversion,” IEEEPhoton. Technol. Lett. **7**(3), 327–329 (1995).

42. J. Hansryd, F. Dross, M. Westlund, P. A. Andrekson, and S. N. Knudsen, “Increase of the SBS Threshold in a Short Highly Nonlinear Fiber by Applying a Temperature Distribution,” J. Lightw. Technol. **19**(11), 1691–1697 (2001).

43. F. W. Willems and W. Muys, “Suppression of interferometric noise in externally modulated lightwave AM-CATV systems by phase modulation,” Electron. Lett. **29**(23), 2062–2063 (1993).

44. F. W. Willems, W. Muys, and J. S. Leong, “Simultaneous suppression of stimulated Brillouin scattering and interferometric noise in externally modulated lightwave AM-SCM systems,” IEEE Photon. Technol. Lett. **6**(12), 1476–1478 (1994).

45. P. A. Humblet and M. Azizoglu, “On the bit error rate of lightwave systems with optical amplifiers,” J. Lightw. Technol. **9**(11), 1576–1582 (1991).

46. M. Barozzi and A. Vannucci, “Performance characterization and guidelines for the design of a counter-propagating nonlinear lossless polarizer,” J. Opt. Soc. Am. B **30**(12), 3102–3112 (2013).

47. J. Fatome, S. Pitois, P. Morin, E. Assemat, D. Sugny, A. Picozzi, H. R. Jauslin, G. Millot, V. V. Kozlov, and S. Wabnitz, “A universal optical all-fiber omnipolarizer,” Sci. Rep. **2**(938), 1–8 (2012).

48. A. DeLong, W. Astar, T. Mahmood, and G. M. Carter, “Polarization attraction of 10GBaud NRZ-BPSK signal in a highly nonlinear fiber,” Opt. Exp. **25**(21), 25625–25636 (2017).

49. R.-M. Mu, V. S. Grigoryan, C. R. Menyuk, G. M. Carter, and J. M. Jacob, “Comparison of Theory and Experiment for Dispersion-Managed Solitons in a Recirculating Fiber Loop,” IEEE J. Sel. Topics Quantum Electron. **6**(2), 248-257 (2000).

50. J. P. Gordon and L. F. Mollenauer, “Phase noise in photonic communications systems using linear amplifiers,” Opt. Lett. **15**(23), 1351-1353 (1990).

51. H. Kim, and A. H. Gnauck, “Experimental Investigation of the Performance Limitation of DPSK Systems Due to Nonlinear Phase Noise,” IEEEPhoton. Technol. Lett. **15**(2), 320–322 (2003).

52. A. H. Gnauck, and P. J. Winzer, “Optical Phase-Shift-Keyed Transmission,” J. Lightw. Technol. **23**(1), 115–130 (2005).

53. Y.-J. Qiao, J. Zhou, W.-H. Qian, and Y.-F. Ji, “The Gordon-Mollenauer Effect in 112 Gbit/s DP-QPSK Systems,” Chin. Phys. Lett. **30**(8), 084203 (2013).

54. G. M. Carter, H. Xu, H. Jiao, Y. Sun, B. S. Marks, and L. Yan, "Effects of polarization dependent loss and polarization mode dispersion in recirculating loops," in Proceedings of Lasers and Electro-Optics Society, 2003 (IEEE 2003), pp. 322–323.

55. G. M. Carter and Y. Sun, "Making the Q distribution in a recirculating loop resemble a straight line distribution," in Proceedings of Optical Fiber Communication Conference and Exhibit, 2002 (IEEE 2002), pp. 509–510.

56. G. P. Agrawal, *Nonlinear Optics* (Academic, 2001), Chap. 5.

57. P. J. Winzer, A. H. Gnauck, S. Chandrasekhar, S. Draving, J. Evangelista, and B. Zhu, “Generation and 1,200 km transmission of 448-GBs ETDM 56-GBaud PDM 16-QAM using a single IQ modulator,” in Proceedings of Optical Communication (ECOC), 2010 36th European Conference and Exhibition on (IEEE 2010), pp. 1–3.

58. K.-P. Ho and J. M. Kahn, "Electronic compensation technique to mitigate nonlinear phase noise," J. Lightw. Technol., **22**(3), 779–783 (2004).

59. A. Carena, V. Curri, G. Bosco, P. Poggiolini, and F. Forghieri, "Modelling of the impact of nonlinear propagation effects in uncompensated optical coherent transmission links," J. Lightw. Technol. **30**(10), 1524–1539 (2012).

60. S. Saito, T. Imai, T. Sugie, N. Ohkawa, Y. Ichihasi, and T. Ito, "Coherent transmission experiment over 2,223 km at 2.5 Gbit/s using erbium-doped fibre amplifiers," Electronics Lett. **26**(10), 669-671 (1990).

61. S. Kumar, "Analysis of nonlinear phase noise in coherent fiber-optic systems based on phase shift keying," J. Lightw. Technol. **27**(21), 4722–4733 (2009).

62. S. Kumar and M. J. Deen, *Fiber Optic Communications, Fundamentals and Applications* (John Wiley & Sons, 2014), Chap. 10.

63. Y. Sun, A. O. Lima, I. T. Lima, Jr., J. Zweck, L. Yan, C. R. Menyuk, and G. M. Carter, “Statistics of the System Performance in a Scrambled Recirculating Loop with PDL and PDG,” IEEEPhoton. Technol. Lett. **15**(8), 1067–1069 (2003).

64. A. H. Gnauck, P. J. Winzer, S. Chandrasekhar, X. Liu, B. Zhu, and D. W. Peckham, “Spectrally Efficient Long-Haul WDM Transmission Using 224-GBaud Polarization-Multiplexed 16-QAM,” J. Lightw. Technol. **29**(4), 373–377 (2011).

65. P. Minzioni, V. Pusino, I. Cristiani, L. Marazzi, M. Martinelli, and V. Degiorgio, “Study of the Gordon-Mollenauer Effect and of the Optical-Phase-Conjugation Compensation Method in Phase-Modulated Optical Communication Systems,” IEEE Photon. J., **2**(3), 284–291 (2010).

66. T. Kurosu, H. N. Tan, K. Solis-Trapala, and S. Namiki, “Signal phase regeneration through multiple wave coherent addition enabled by hybrid optical phase squeezer,” Opt. Exp. **23**(21), 27920–27930(2015).

67. R. Slavik, F. Parmigiani, J. Kakande, C. Lundstrom, M. Sjodin, P. A. Andrekson, R. Weerasuriya, S. Sygletos, A. D. Ellis, L. Gruner-Nielson, D. Jakobsen, S. Herstrom, R. Phelan, J. O’Gorman, A. Bogris, D. Syvridis, S. Dasgupta, P. Petropoulos, and D. J. Richardson, “All-optical phase and amplitude regenerator for next-generation telecommunications systems,” Nature Photon. **4**(10), 690–695 (2010).

68. S. Boscolo, S. K. Turitsyn, and K. J. Blow, “Nonlinear loop mirror-based all-optical signal processing in fiber-optic communications,” Opt. Fiber Technol. **14**(4), 299–316 (2008).

69. A. Almaiman, Y. Cao, M. Ziyadi, A. Mohajerin-Ariaei, P. Liao, C. Bao, F. Alishahi, A. Fallahpour, B. Shamee, N. Ahmed, A. J. Willner, Y. Akasaka, T. Ikeuchi, S. Takasaka, R. Sugizaki, S. Wilkinson, J. D. Touch, M. Tur, and A. E. Willner, “Experimental demonstration of phase-sensitive regeneration of a binary phase-shift keying channel without a phase-locked loop using Brillouin amplification,” Opt. Lett. **41**(23), 5434-5437 (2016).

70. T. Kurosu, M. Gao, K. Solis-Trapala, and S. Namiki, “Phase regeneration of phase encoded signals by hybrid optical phase sqeezer,” Opt. Exp. **22**(10), 12177-12188 (2014).

71. A. G. Striegler, M. Meissner, K. Cvecek, K. Sponsel, G. Leuchs, and B. Schmauss, “NOLM-Based RZ-DPSK Signal Regeneration,” IEEE Photon. Technol. Lett. **17**(3), 639–641 (2005).

72. J.-W. Goossens, M. I. Yousefi, Y. Jaouen, and H. Hafermann, "Polarization-division multiplexing based on the nonlinear Fourier transform," Opt. Exp. **25**(22), 26437–26452(2017).

73. X. Liu, A. R. Chraplyvy, P. J. Winzer, R. W. Tkach, and S. Chanrasekhar, "Phase-conjugated twin waves for communication beyond the Kerr nonlinearity limit," Nature Photonics **7**(7), 560–569 (2013).

74. P. Poggiolini, G. Bosco, A. Carena, V. Curri, F. Forghieri, "Performance evaluation of coherent WDM PS-QPSK (HEXA) accounting for non-linear fiber propagation effects," Opt. Exp. **18**(11), 11360–11371(2010).

75. A. Mecozzi, "Limits to long-haul coherent transmission set by the Kerr nonlinearity and noise of the in-line amplifiers," J. Lightw. Technol. **12**(11), 1993–2000 (1994).

76. K.-P. Ho, "Statistical properties of nonlinear phase noise," https://arxiv.org/pdf/physics/0303090.

77. Y. C. Eldar, A. V. Oppenheim, and D. Egnor, "Orthogonal and projected orthogonal matched filter detection," Signal Process. **84**(4), 677-693 (2004).